Chapter 6 – Calculation of High Pressure Ion and Neutral Energy Distributions

6.1 Introduction

Chapter 6 contains an extension to the IED simulation model described in Chapter 5 to include collisional effects within the sheath. Most RIE processes have been developed in the pressure range of 10-100 mTorr; hence if IED simulations are to be applicable to real etch processes the phenomena occurring in a sheath at these increased pressures need to be included in the model of ion trajectories. The *high pressure* regime shall be defined for the purposes of IED calculations as between 10 mTorr and 1 Torr.

The theory used to model collisional processes in Ar plasmas will first be described and then examples of high pressure IEDs will be given for various plasma conditions. IEDs will then be compared to experimental distributions measured at both the cathode and anode during high pressure etch processes.

The method used to calculate the energy distribution of neutral particles (in this case Ar atoms) striking the cathode will then be described, and several neutral energy distributions will be presented. Inelastic collision processes will also be investigated briefly. Finally the energy distribution of fast atoms leaving the sheath and entering the plasma region will be presented.

6.2 Collisional Processes within the Sheath

As the pressure of an RF discharge increases, the mean free path of ions and atoms decreases. When the mean free path of ions travelling through the sheath region becomes commensurate with the sheath thickness, ion trajectories cease to be ballistic and collisions begin to occur between the ion and gas molecules. These collisions can significantly affect ion trajectories and energies, and so collisions will have a major influence upon observed IEDs and IADs. For a typical complex gas plasma (such as CF_4 or SF_6), the number of processes occurring when a molecule is struck by a fast positive ion can be very varied and include phenomena such as dissociation, rovibrational excitation, electronic excitation and chemical reactions of many types. To model one of these complex process gases, therefore, accurate knowledge of the cross-sections for every important collisional process that could occur would be required. This information would be needed for each ion/neutral pair, along with the distribution function for the impact energy into post-collisional products. These data are not, in general available, and moreover are not readily estimated. Consequently, the system to be studied must be simplified into interactions that can be readily modelled.

Therefore, it was decided to restrict the model to Ar, since in such simple, monatomic, inert gas plasmas there are only two interactions which significantly affect the IED, namely scattering and charge exchange. Each of these interactions has its own cross-section and dependence upon energy, and affects the IED in a different way. For the purposes of modelling sheath interactions it has been assumed that scattering and charge exchange can be separated into two independent processes which do not affect one another. Furthermore, since Ar can be taken to be effectively

spherical, collisional processes can be treated as isotropic, with no preferred ion-atom collision orientation.

The degree of complexity of the model for collisions will be increased gradually throughout this Chapter, but to begin with let us assume that all Ar^+/Ar collisions are elastic (*i.e.* no ion kinetic energy is converted into electronic excitation of either the ion or atom), isotropic, and consist of only the two processes mentioned above.

The model for collisional sheaths used in this thesis builds upon ion trajectory studies performed by other workers. There have been several major publications on the theoretical study of higher pressure RF sheaths [126,127,138,139]. Kushner [138] modelled Ar^+ ion trajectories for various different plasma conditions, including the variation of ionic mean free path (*i.e.* pressure). However, only charge exchange interactions were included in his work. Wild and Koidl [126] measured IEDs in Ar discharges and successfully predicted the energies of peaks in the IED using a model for charge exchange in the sheath. Thompson *et al* [139] modelled collisional ion trajectories including both scattering and charge exchange phenomena. They also introduced an energy dependent ionic collision cross-section. Although all of these reports provide a detailed description of the ion dynamics in the sheath, they do not attempt to place the calculations in the context of a realistic RF etch system. Sawin *et al* [127] have simulated IEDs and IADs for Ar^+ ions striking the anode of an RF reactor, and then directly compared these simulations to experimental results. However, their use of an unrealistic description of the sheath potential has limited the accuracy of their computed IEDs, and therefore they only obtain an underlying qualitative resemblance to their experimental results.

The work reported in the following sections is (to the author's knowledge) the first attempt to perform calculations in a high pressure RF discharge, incorporating both a realistic description of the time-varying fields in the system and an adequate model of the collisions in the sheath.

We shall begin by considering scattering and charge exchange effects separately, then look at the combined effects of both processes upon an IED. Finally, predicted high pressure IEDs will be compared with experimental observation.

6.2.1 Elastic Scattering

This process involves both momentum and energy transfer between the ion and atom. Compared to the large velocity of the ion, an atom which is in thermal equilibrium with the bulk gas at a temperature of about 300 K can be considered to be effectively stationary. Ar ions and atoms are taken to be hard spheres that undergo elastic collisions. This hard-sphere scattering model has been adopted as an acceptable approximate method, in which hard-sphere dynamics are employed in conjunction with an energy dependent cross-section. This model is referred to as the *isotropic shrinking sphere model* by Thompson *et al* [139]. In that work, the authors showed that using such an approximation gave results that exhibited no important differences in behaviour from models that employed either a pure hard-sphere or a 9-6-4 interaction potential. Therefore, this shrinking hard sphere approximation was used in all the calculations described in the following sections in order to make the best use of computing time while still obtaining accurate results.

The collision model is that of a positive ion of mass, m_1, moving with velocity, v_0, colliding with a stationary atom of mass, m_2. The ion trajectory then undergoes an instantaneous change

in direction, with the ion now leaving with velocity, v_1, at an angle, γ, to its original direction of motion. The atom recoils with velocity, v_2, at an angle, β, to the original direction of motion of the ion (see fig.6.1).

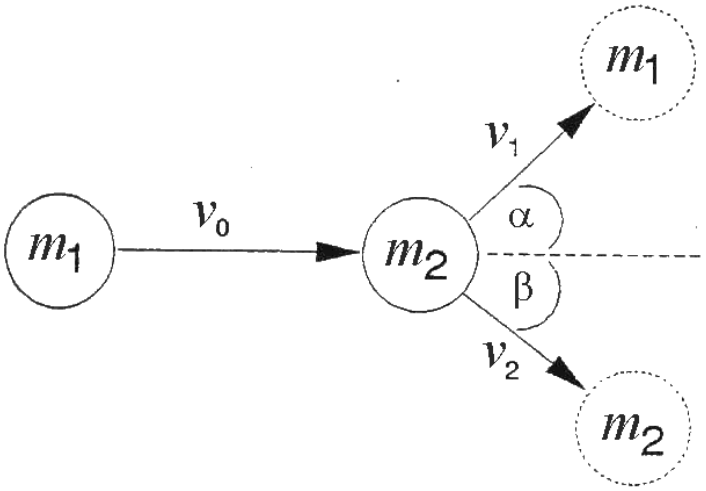

Fig. 6.1. Hard sphere isotropic scattering.

By conservation of energy and momentum it can be shown [188] that

$$v_1/v_0 = \{\cos\gamma \pm (\alpha^2 - \sin^2\gamma)^{1/2}\} / (1+\alpha) \qquad (6.1)$$

where

$$\alpha = m_2 / m_1 \qquad (6.2)$$

and

$$v_2 = 2v_0 \cos\beta / (1+\alpha) \qquad (6.3)$$

There are three cases of interest:

(a) $\boldsymbol{m_1 = m_2}$, *i.e.* $\alpha = 1$: This is the case for an Ar plasma, where Ar^+ and Ar effectively have identical masses. Also, for this case we have $\gamma + \beta = 90°$. Therefore, Equations (6.1) and (6.3) reduce to

$$v_1 = v_0 \cos\gamma \qquad (6.4)$$

$$v_2 = v_0 \sin\gamma \qquad (6.5)$$

(b) $\mathbf{m_2 \geq m_1}$, *i.e.* $\alpha \geq 1$: This would be the case for H^+ ions striking Ar atoms. Since momentum transfer is now inefficient, the heavy atoms do not recoil greatly. Hence, the ion will scatter with a large proportion of its initial energy. The scattering angle, γ, can vary from 0° to 180°, indicating that for head-on collisions the ion can reflect off the heavy atom

directly back along its original path.

(c) $m_2 < m_1$, *i.e.* $\alpha < 1$; This would be the case for Ar^+ ions scattering off H atoms. Conservation of momentum shows that the maximum scattering angle possible in this case is given by $\sin \gamma < \alpha$. This means that forward scattering always occurs.

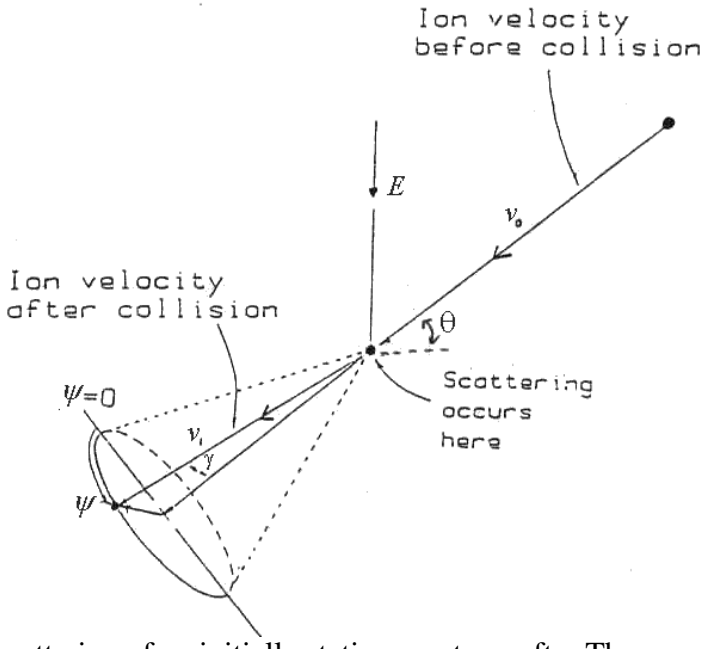

Fig.6.2a. Ions scattering of an initially stationary atom, after Thompson *et al* [139]. The final trajectory of the atom is not shown.

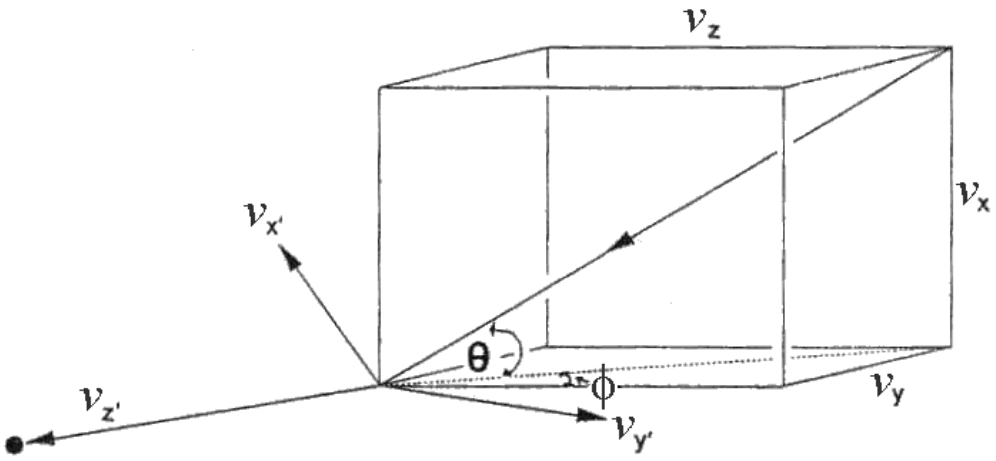

Fig.6.2b. Co-ordinate system for scattering. v_x, v_y, v_z, are the pre-collision ion velocity components, and v_x', v_y' and v_z' are the post-collision velocity components.

For Ar plasmas, case (a) is the relevant one. Since we are assuming isotropic scattering, there is another angle which needs to be considered. This angle is the azimuthal angle ψ and is

independent of the values of v_0 or γ. The relationship between γ and ψ can be seen in fig.6.2a. However, γ and ψ are defined relative to the initial direction of the ion velocity. In order to continue to follow the ion trajectory in the sheath after the collision, we need to convert the velocity of the ion from these polar coordinates (v_1, γ, ψ) into the rectilinear (x, y, z) coordinates relative to the electrode. This procedure is performed in two stages.

Stage 1. Convert polar coordinates to rectilinear: these rectilinear coordinates will also be relative to the initial ion velocity vector. The new velocity coordinates v_x', v_y', and v_x' are mutually orthogonal and are defined such that v_z' is in the same direction as v_0. We then have

$$v_x' = v_1 \sin\gamma \cos\psi \tag{6.6}$$
$$v_y' = v_1 \sin\gamma \sin\psi \tag{6.7}$$
$$v_z' = v_1 \cos\gamma \tag{6.8}$$

Stage 2. Rotate the coordinate system: the initial ion velocity vector with components v_x, v_y and v_z was defined relative to the electrode, where v_x was perpendicular to the electrode. The impact angle, θ, is the angle between the original ion velocity vector, and the electrode, and is given by Equation (5.12). The angle ϕ is the angle between the projection of v_0 onto the yz plane and the z direction (see fig.6.2b). Hence, ϕ is given by

$$\tan\phi = v_y / v_z \tag{6.9}$$

To convert v_x', v_y' and v_z' to the coordinate system of v_x, v_x, and v_x, we need to rotate the velocity component vectors by θ and ϕ such that

$$v_x = -v_x' \cos\theta + v_z' \sin\theta \tag{6.10}$$
$$v_y = v_y' \cos\phi + v_z' \cos\theta \sin\phi + v_x' \sin\theta \sin\phi \tag{6.11}$$
$$v_z = v_y' \sin\phi - v_z' \cos\theta \cos\phi - v_x' \sin\theta \cos\phi \tag{6.12}$$

So, for any scattering angles γ and ψ, by the use of Equations (6.6) to (6.12) we can now obtain the post-collision ion velocity components in the reactor coordinate system. However, we still require a method of randomly choosing γ and ψ.

6.2.2 Choosing the Scattering and Azimuthal Angles

McDaniel [189] shows that the probability, P, of a sphere being scattered into an angle, γ, after a collision with a sphere of identical size is given by

$$P(\gamma) = v_1 m_1 \sin\gamma / (v_0 \mu) \tag{6.13}$$

where μ is the reduced mass of the system given by

$$\mu = m_1 m_2 / (m_1 + m_2) \tag{6.14}$$

and since v_1 is given by Equation (6.1), we get for the general case

$$P(\gamma) = \{(\cos\gamma \pm (\alpha^2 - \sin^2\gamma)^{1/2}) / (1 + \alpha)\}\, m_1 \sin\gamma / (v_0\, \mu) \tag{6.15}$$

For the three cases considered previously, we get [189]

(a) $\boldsymbol{m_1 = m_2}$: the probability of being scattered into an angle γ is

$$P(\gamma) = \sin 2\gamma \qquad \text{where } 0° < \gamma < 90° \tag{6.16}$$

Following the procedure described in Appendix III which describes the method for choosing a random value for a variable, x, given a probability distribution, $P(x)$, we get that

$$P(\gamma) = \tfrac{1}{2} \cos^{-1}(1 - 2R) \tag{6.17}$$

where R is a random number chosen between 0 and 1.

(b) $\boldsymbol{m_1 << m_2}$: here we have

$$P(\gamma) = \tfrac{1}{2} \sin\gamma \qquad \text{where } 0° < \gamma < 180° \tag{6.18}$$

so that γ is chosen from

$$P(\gamma) = \cos^{-1}(1 - 2R) \tag{6.19}$$

(c) $\boldsymbol{m_1 >> m_2}$: this gives

$$P(\gamma) = \tfrac{1}{2} \sin\gamma \qquad \text{where } 0° < \gamma < \sin^{-1}\alpha \tag{6.20}$$

so that γ is chosen from

$$P(\gamma) = \cos^{-1}(1 - 2R) \tag{6.21}$$

In this last case we have to constrain γ to lie between 0° and $\sin^{-1}\alpha$. Hence, R is chosen between 0 and R_{max}, where $R_{max} = \tfrac{1}{2}\{ (1 - (1 - \alpha^2)^{1/2}$.

The azimuthal angle, ψ, is independent of the details of the impact, and since we are assuming isotropic scattering, ψ can take any value between 0 and 2π radians. So we choose ψ from

$$\psi = 2\pi R \tag{6.22}$$

where, again, R is another random number between 0 and 1.

We are now in a position to calculate the scattering angles γ and ψ of the ion based upon the collision dynamics, and then obtain the post-collision ion trajectory. In passing it is worth noting that the trajectory of the atom can also be followed, and this is discussed in section 6.10.

6.2.3 Charge Exchange

Charge exchange is treated as a process that does not involve momentum or energy transfer. As the fast-moving positive ion passes near an effectively stationary atom, an electron from the atom transfers to the ion, neutralising it. After the interaction, the newly-created neutral atom continues on its previous trajectory unaffected by the presence of any sheath potential. The atom that lost the electron has now become a positive ion that is initially drifting at thermal equilibrium with the bulk gas, and so has a typical kinetic energy of about 0.04 eV. This new ion will continue to drift at the thermal velocity until the next expansion of the sheath envelops it, at which point the ion will experience a force towards the electrode. Since this ion was created somewhere between the plane of origin and the electrode, it will strike the electrode with less energy than those ions that experienced the sheath potential over the whole sheath thickness. The initial x,y,z velocity components for the new ion are chosen randomly by a Monte Carlo technique (see Appendix III) in such a way as to be consistent with a Maxwell-Boltzmann distribution having a mean of 0.04 eV (or any chosen value). The subsequent trajectory of the ion is then followed from the point of charge exchange until it either strikes the electrode or undergoes another collision.

6.2.4 Determination of the Ionic Mean Free Path

We are now in possession of models for the collision dynamics for both scattering and charge exchange. However, we still need a method to determine at what point in the trajectory a collision occurs. This point will be a random function determined by the mean free path of the ion in the gas. The mean free path, λ_0, of a species through a gas of density n is given by [165]

$$\lambda_0 = 1 / (\sqrt{2}\, \sigma n) \qquad (6.23)$$

where σ is the collision cross-section. If one species is treated as being stationary, then this equation reduces to

$$\lambda_0 = 1 / (\sigma\, n) \qquad (6.24)$$

The probability, P, that a species of mean free path λ_0 moves a distance x before undergoing a collision is given by [189]

$$P(x) = (1 / \lambda_0) \exp (- x / \lambda_0) \qquad (6.25)$$

Using the method described in Appendix III, we can choose a random collision distance x_{coll} based upon this probability distribution from

$$x_{coll} = -\lambda_0 \ln(1 - R) \tag{6.26}$$

where R is a random number chosen between 0 and 1.

In order to use Equation (6.26) we need a value for σ for both scattering and charge exchange processes. These cross-sections are then simply added together to obtain the total cross-section σ_t, so that

$$\sigma_t = \sigma_e + \sigma_s \tag{6.27}$$

where σ_e and σ_s are the cross-sections for charge exchange and scattering, respectively. However, there is an immediate problem; collision cross-sections are usually dependent upon the total kinetic energy of the collision species. For the Ar^+/Ar system, the values of σ_e, σ_s and σ_t have been measured by Cramer [190] and are given in fig.6.3. These measurements are particularly useful since they not only cover the energy range found in typical RIE sheaths (1-400 eV), but they also show *both* the cross-section for scattering *and* charge exchange obtained using the same experimental conditions. Hence, even though there might still be a systematic error in the absolute magnitudes of these cross-section values, the ratio of the two should be reasonably accurate.

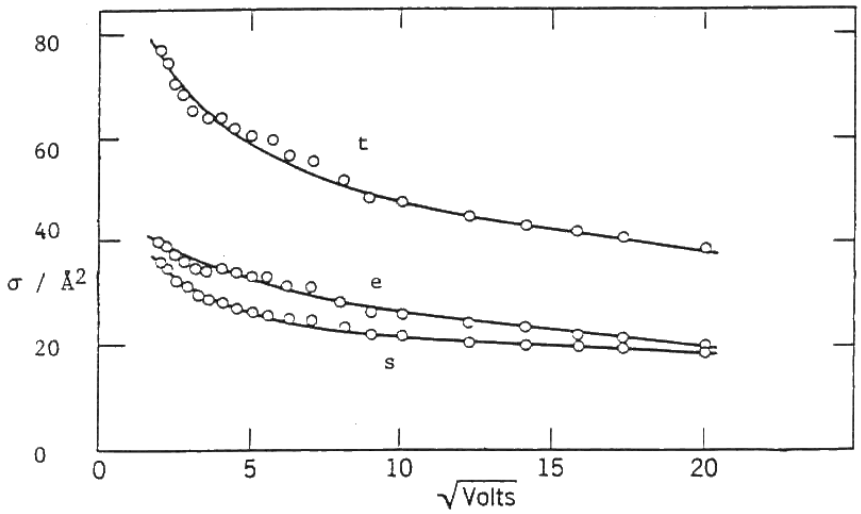

Fig.6.3. Scattering (s), charge exchange (e) and total (t) cross-sections for Ar^+ in Ar (after Cramer [190]) as a function of collision kinetic energy. The horizontal axis is proportional to the square root of the energy, *i.e.* the ion velocity.

It should be noted that other measurements of a for Ar^+/Ar (*e.g.* ref.[191]) give values that can be up to 5 times less than those quoted by Cramer. Although these were often earlier measurements, they still highlight the problem that the absolute magnitudes of collision cross-sections are still not known very accurately. Another problem is that Cramer's measurements

start at about 1 eV, which means that for collisions with energy < 1 eV the cross-section must be estimated, leading to a possible source of error. This is particularly troublesome since the curves in fig.6.3 appear to be rising rapidly as the energy decreases. Hopefully, this should not affect simulations of IEDs significantly, since such low energy species are not of great interest in the study of etching mechanisms.

In order to use these cross-section data, the curves depicted in fig.6.3 have been fitted to linear expressions. More complex fitting routines (splines, polynomials *etc*.) were not used because the values of a were deemed insufficiently accurate to warrant more than a simple fitting routine. It has been shown [191] that for some measurements of a an expression like $(\sigma)^{1/2} = A + B \ln(v)$, where v is the collision velocity, can be used to fit the data. However, it was decided that a simple linear fit was much faster to calculate, so speeding up computer time. The fitting equations used were as follows, and give σ in units of $Å^2$.

(a) **Scattering**

$$\sigma_s = -0.36\,(eV)^{1/2} + 25 \qquad \text{for } eV > 49 \qquad (6.28)$$

$$\sigma_s = -3.30\,(eV)^{1/2} + 43 \qquad \text{for } eV \le 49 \qquad (6.29)$$

(b) **ChargeExchange**

$$\sigma_e = -0.72\,(eV)^{1/2} + 34 \qquad \text{for } eV > 49 \qquad (6.30)$$

$$\sigma_e = -1.90\,(eV)^{1/2} + 43 \qquad \text{for } eV \le 49 \qquad (6.31)$$

(c) **Total**

$$\sigma_t = -1.08\,(eV)^{1/2} + 59 \qquad \text{for } eV > 49 \qquad (6.32)$$

$$\sigma_t = -5.20\,(eV)^{1/2} + 86 \qquad \text{for } eV \le 49 \qquad (6.33)$$

The fitting expressions are used to extrapolate cross sections back to the $\sqrt{V} = 0$ axis and give a value of 86 $Å^2$ for the maximum interaction cross section of Ar^+ ions in Ar gas. This value is denoted σ_{max} and corresponds to an effective collision diameter for Ar^+ ions of 5.2 Å. The curves in fig.6.3 show that λ_0 is energy dependent and thus x_{coll} in Equation (6.26) is also energy dependent. Therefore, as an ion accelerates, its probability of undergoing a collision decreases.

In order to incorporate this shrinking sphere effect into our model, the approach outlined by Thompson *et al* [139] is adopted. Firstly, the mean free path is calculated from Equation (6.24) using a value for the cross-section of $\sigma = \sigma_{max}$. Then Equation (6.26) is used to determine the collision distance x_{coll}. The ion trajectory is then followed until the ion has travelled a total distance of x_{coll}. At this point, we determine whether a collision would actually take place, taking into account that the real cross-section would now be reduced due to the ion acquiring kinetic energy on its journey. We therefore calculate the probability that the ion still undergoes an interaction, given its now reduced cross-section. The probability of interaction, P, is given by the ratio of the real cross-section at an ion energy of E, to the maximum, so that

$$P(\text{collision}) = \sigma_t(E) / \sigma_{max} \qquad (6.34)$$

We now choose a random number, R, between 0 and 1, and compare this to the value of P.

If $R > P$, no collision occurs, and the ion continues on unaffected. A new value of x_{coll} is now

randomly chosen using Equation (6.26) and $\sigma = \sigma_{max}$. The ion trajectory is then followed until it either strikes the electrode or has travelled a distance of x_{coll}, whereupon the test for collision is repeated.

If $R \leq P$, then a collision is deemed to have occurred and we now need to decide which of the two types of collision processes took place. The probability of each type of process is given simply by the ratio of its cross-section to the total cross-section. Thus, the probability of scattering is

$$P(\text{scattering}) = \sigma_s(E) / \sigma_t(E) \tag{6.35}$$

and that of charge exchange will be

$$P(\text{charge exchange}) = 1 - P(\text{scattering}) \tag{6.36}$$

A second random number, R_1 is now chosen between 0 and 1. By comparing R_1 to the probabilities calculated from Equations (6.35) and (6.36), the type of collision process can then be determined.

Ion trajectories are followed until they suffer one of three fates.

(i) They either strike the electrode, at which point their energy and angle of impact are stored in an array in the computer memory to form the IED and IAD.

(ii) Alternatively, as a result of scattering, an ion may be travelling in such a direction ($v_x < 0$) that it passes back through the plane of origin to re-enter the plasma region. The subsequent trajectory of this *backscattered* ion is then ignored by the program and a new ion is chosen from the initial starting conditions.

(iii) Finally the ion may travel a distance of x_{coll} and possibly undergo another collision. At higher pressures, ions may experience many sequential collisions (both scattering and charge exchange) on their passage from the plane of origin to the electrode.

6.2.5 Monte Carlo Simulations of Collisions

To implement collisional processes in the Monte Carlo IED simulation program, it was necessary to incorporate a few extra routines into the computer code. The flow diagram for the new program (NED FORTRAN) is shown in fig.6.4 and a full listing of the program is given in Appendix VII. For high pressure simulations, where the number of collisions within the sheath region becomes large, this program takes about 10 times longer to execute than the low pressure IED simulation.

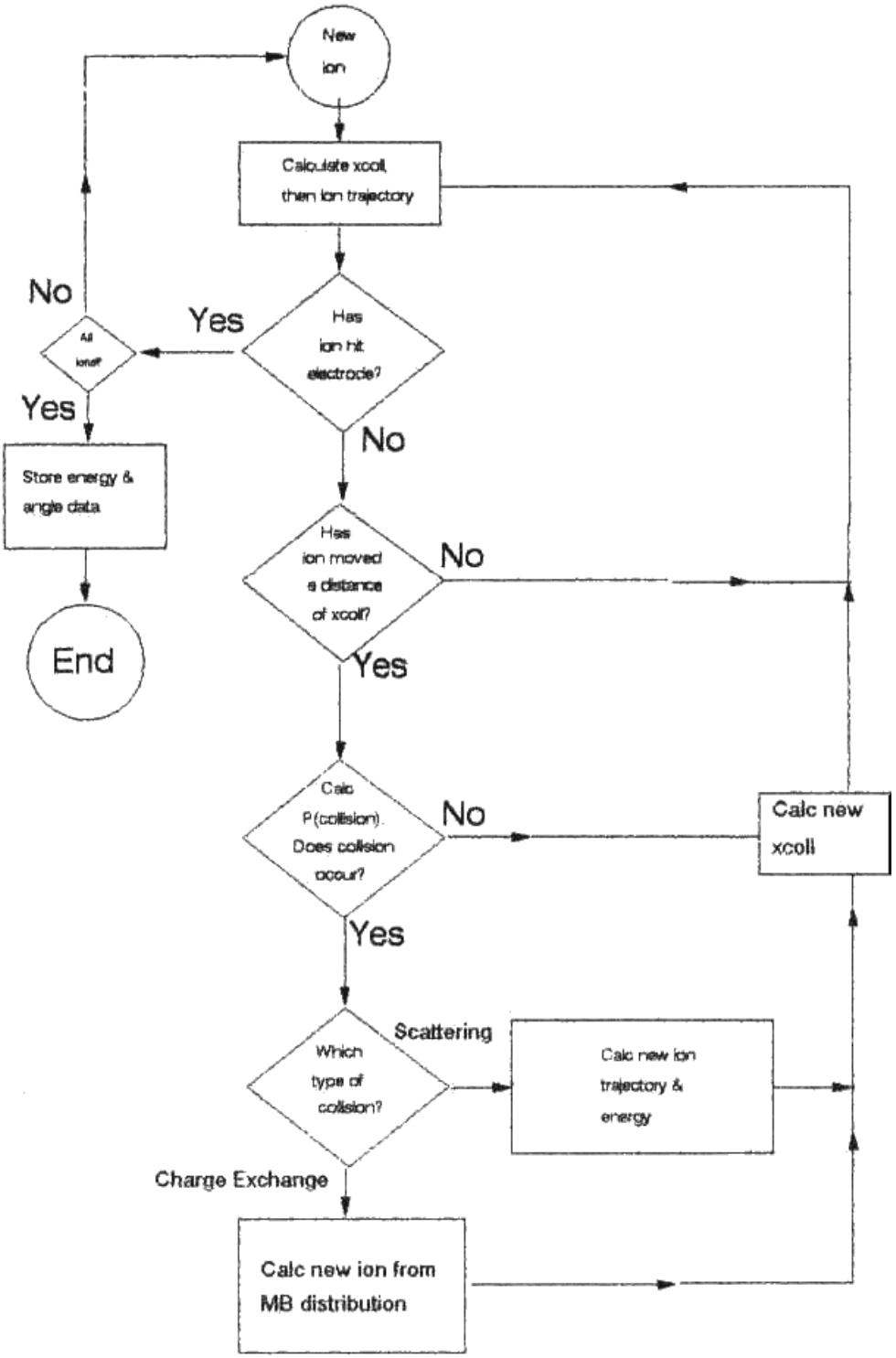

Fig.6.4. Flow chart for high pressure IED simulations. See program NED in Appendix VII.

As with low pressure IEDs, a set of standard plasma conditions was chosen for the high

pressure IED simulation studies. These standard conditions are shown in table 6.1 and are used in all subsequent IED calculations except where specifically stated otherwise. They were chosen to fit experimental data (see section 6.8). The larger number of trajectories required reflects the fact that ions are no longer confined to an energy region between E_1 and E_2, but spread out to lower energies. Hence, in order to maintain an acceptable signal:noise ratio in the IED more trajectories are needed than were used for the low pressure IED simulations. The parameter E_{therm} is discussed in section 6.10.

Pressure	20 mTorr
V_0	356 V
l_{max}	4.69 mm
A_e	0.4
kT_e	1.00 eV
kT_i	0.05 eV
Frequency	13.56 MHz
m_{i}	39.948 amu (Ar)
E_{therm}	0.1 eV
No. trajectories	25000
Time increment	5×10^{-10} s
Electrode	Cathode

Table 6.1. The standard high pressure plasma conditions used for IED and IAD simulations.

In order to understand the relative contributions of scattering and charge exchange to IEDs and IADs, the two processes shall now be separated and studied individually.

6.3 The Effect of Scattering Upon IEDs and IADs

To begin with, let us examine the effects upon IEDs of just scattering, in the absence of charge exchange. Collisions that would normally have produced a charge exchange interaction have been treated here in a manner identical to a non-collision, *i.e.* a new value of x_{coll} is chosen and the ion continues along its pre-collision trajectory unaffected. IEDs including scattering processes only are shown in fig.6.5(a-f) for pressures ranging from 1 to 100 mTorr. The main effect of scattering is a gradual smearing of the IED to lower energies. This is illustrated by a low energy tail developing as the pressure increases. This tail increases in size relative to the original double-peaked distribution until by 50 mTorr (fig.6.5e) the original IED is barely distinguishable above the tail. At 100 mTorr the IED has been completely blurred into a broad spread of energies with no sign of the original distribution remaining.

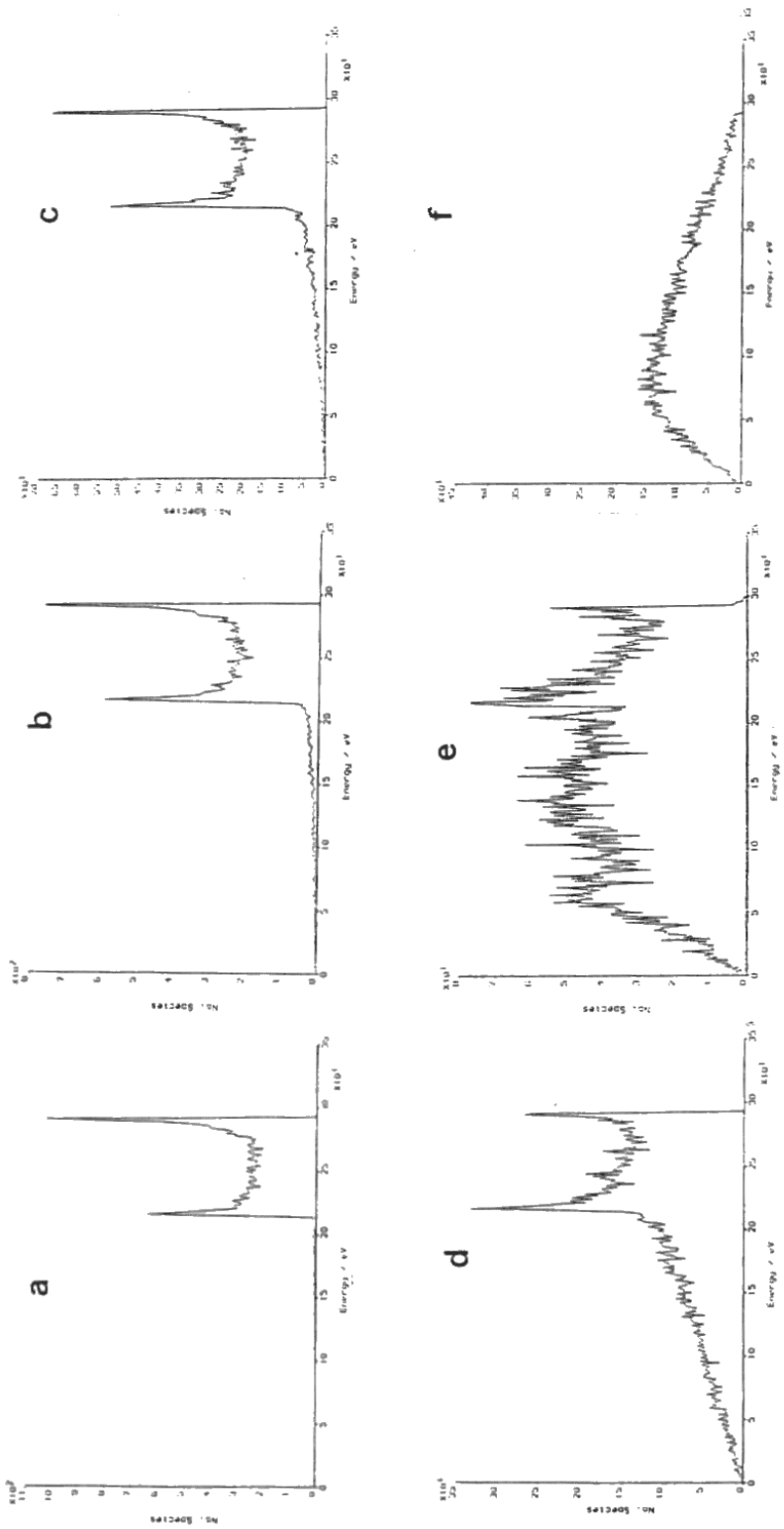

Fig.6.5. IEDs calculated using the standard high pressure plasma conditions incorporating scattering processes only, for pressures of (a) 1, (b) 5, (c) 10, (d) 30, (e) 50 and (f) 100 mTorr.

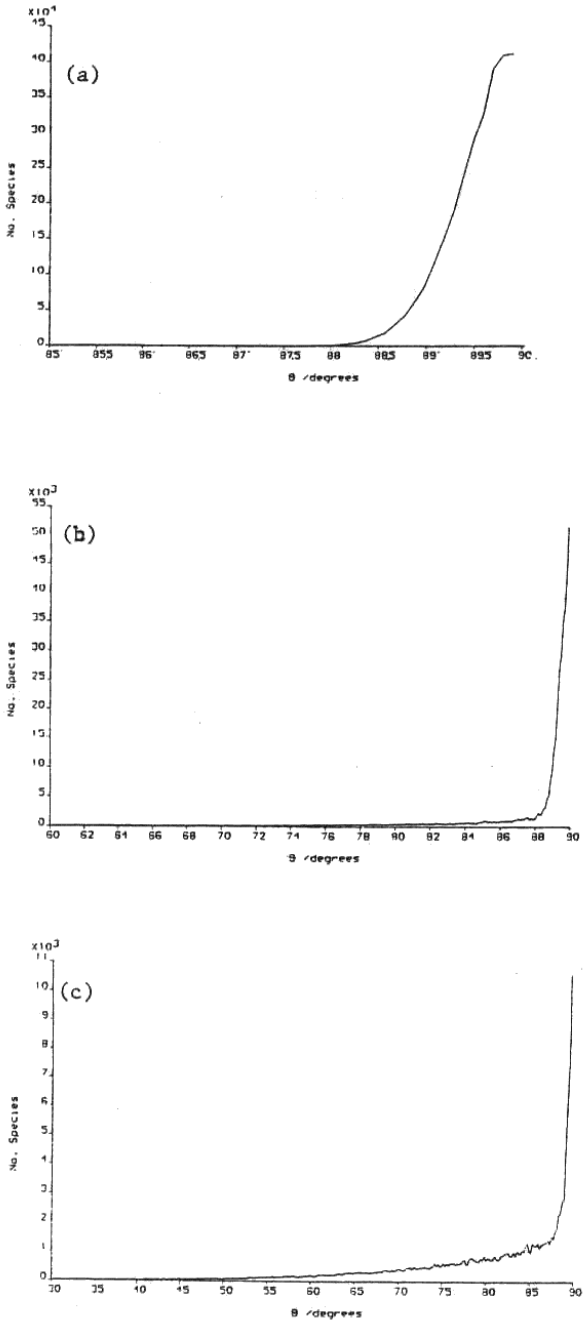

Fig.6.6. IADs corresponding to the conditions of fig.6.5, except at pressures of (a) 1, (b) 50 and (c) 100 mTorr.

Fig.6.6(a-c) show the IADs for the same set of process conditions. Note that the convention used throughout this Chapter concerning IADs is the same as that described in fig.5.4, namely the impact angle is defined such that 0° is parallel to the electrode and 90° is

normal incidence. Also, as in Chapter 5, IADs have been normalised to equal solid angle by multiplying the vertical axis by cos θ.

Referring to fig.6.6, at low pressures with few collisions in the sheath, ion trajectories are unimpeded, and so all the ions strike the electrode at near normal angles of incidence ($\theta > 88°$). As the pressure increases and scattering collisions deflect the ions away from normal incidence, ions start to strike the electrode at increasingly shallower angles. At 100 mTorr (fig.6.6c), many ion trajectories are now deflected away from normal incidence, with ions striking the surface at angles down to 30°.

Consequently, scattering in the sheath produces lower energy ions moving at shallower angles.

6.4 The Effect of Charge Exchange Upon IEDs and IADs

We now examine the effect of charge exchange upon IEDs, in the absence of scattering. This is performed in a similar way to that described in section 6.3, only this time scattering is treated as a non-collision. IEDs including charge exchange alone are illustrated in fig.6.7(a-f) and their corresponding IADs in fig.6.8a and b. The IEDs show a startling difference to those seen for scattering alone. At lower pressures the main double-peaked IED dominates the distribution. As the pressure increases, a low energy tail develops in a manner similar to that seen in scattering-only IEDs. However, as the pressure increases still further, this tail develops structure and a series of secondary peaks appear. These secondary peaks are at well-defined energies which are independent of pressure. As the pressure increases, the relative heights of these secondary peaks increases with respect to the main IED. By 50 mTorr, the main IED can only just be distinguished from the secondaries. At pressures of 100 mTorr and above, the main distribution is no longer discernible and the secondary peaks now dominate the IED.

These secondary peaks arise as a direct result of creating new ions at random positions within the sheath. Just as ions that experience the whole sheath potential produce the main IED with definite minimum and maximum energies, so ions formed further into the sheath region will produce their own double-peaked IEDs, but at a lower energy. The secondary IEDs will have a smaller peak separation, ΔE, since these ions will have experienced less of the RF modulation that causes peak splitting, *i.e.* for these ions l_{max} is effectively smaller (see section 5.3.2 which describes the affect of l_{max} upon IEDs). The relative heights of the secondary peaks are directly related to the number of ions undergoing charge exchange at different distances into the sheath.

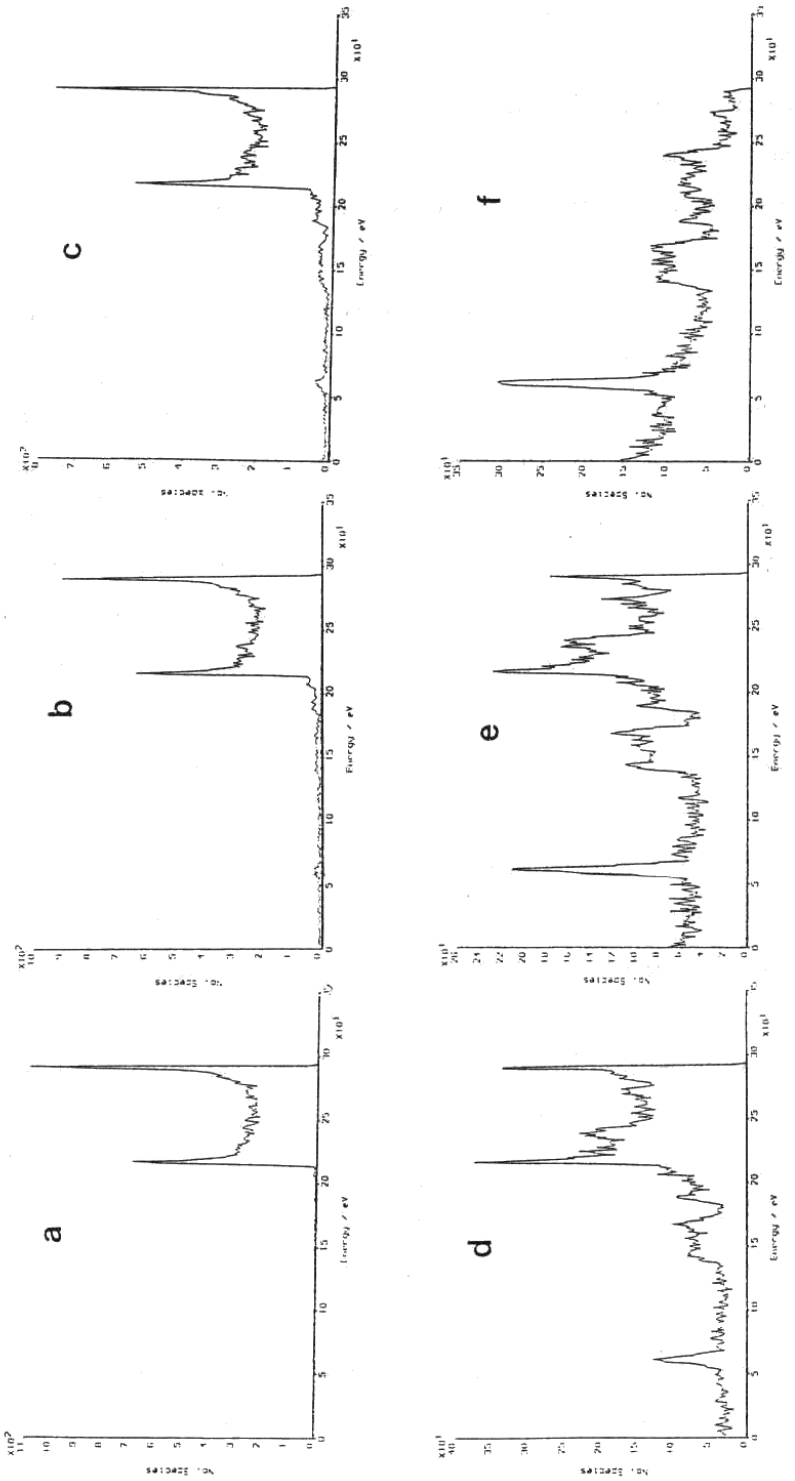

Fig.6.7. IEDs calculated using the standard high pressure plasma conditions incorporating charge exchange processes only, for pressures of (a) 1, (b) 5, (c) 10, (d) 30, (e) 50 and (f) 100 mTorr.

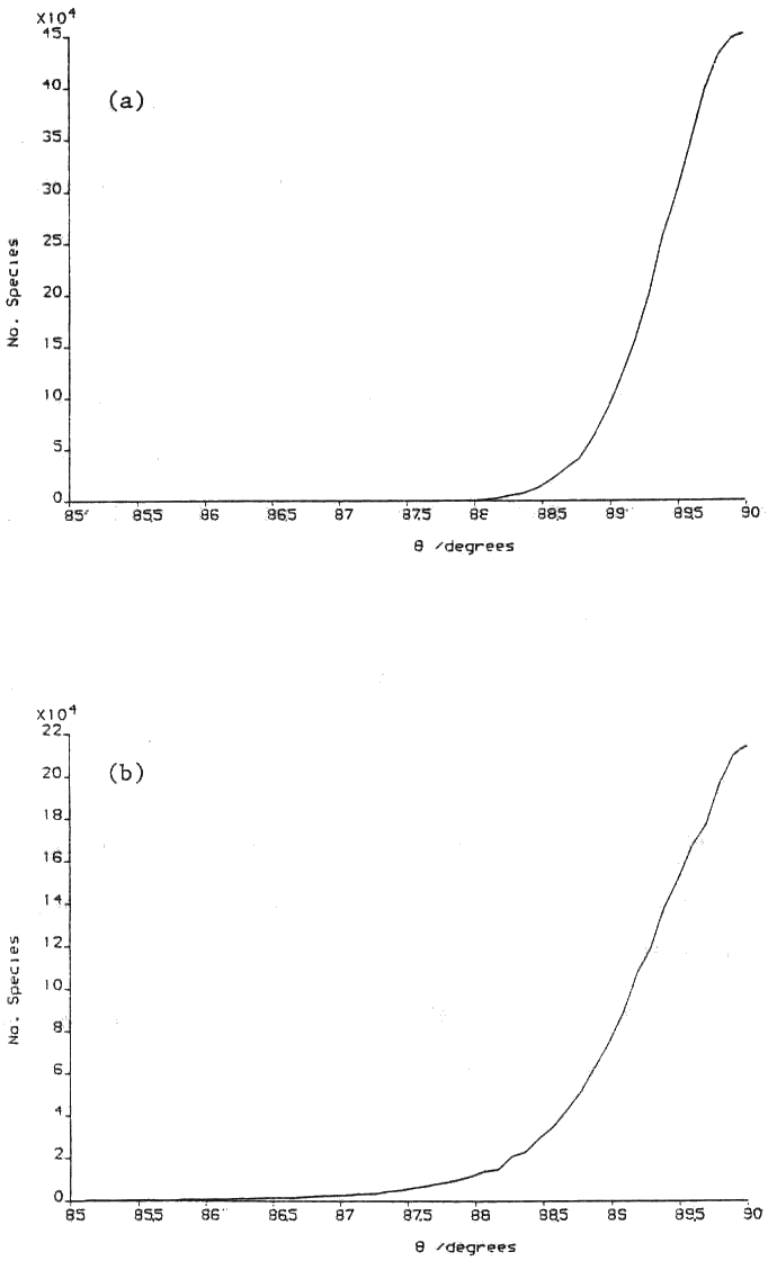

Fig.6.8. IADs corresponding to the conditions of fig.6.7, except at pressures of (a) 1, (b) 100 mTorr.

Fig.6.9 shows an IED calculated for the standard high pressure conditions, except that instead of choosing ions entering the sheath by passing through the plane of origin, ions start at an initially random point chosen between $\lambda = 0$ (the cathode) and $\lambda = l_{max}$ (the plane of origin). This IED shows the secondary peaks at the same energy values as seen in fig.6.7(a-f). A clearer picture of the origin of these peaks can be seen from the illustration in fig.6.10, which shows how the magnitude of ΔE for each of the secondary peaks is related directly to the degree of RF

modulation at the position in the sheath where the ion is created.

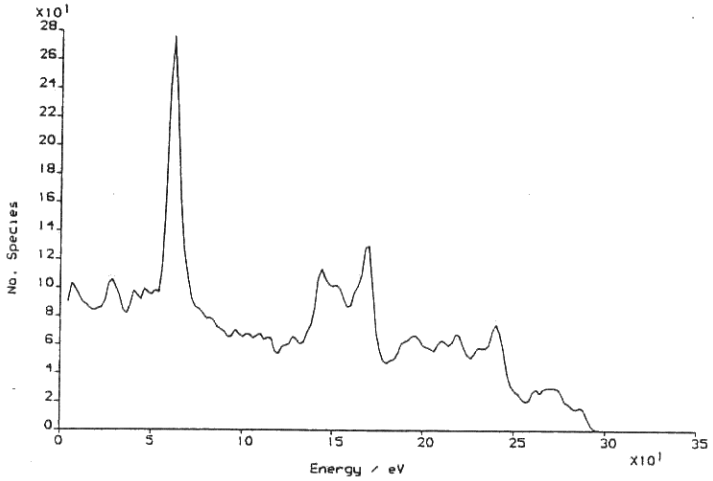

Fig.6.9. IED for ions chosen from random starting positions between the cathode and plane of origin for the standard high pressure plasma conditions.

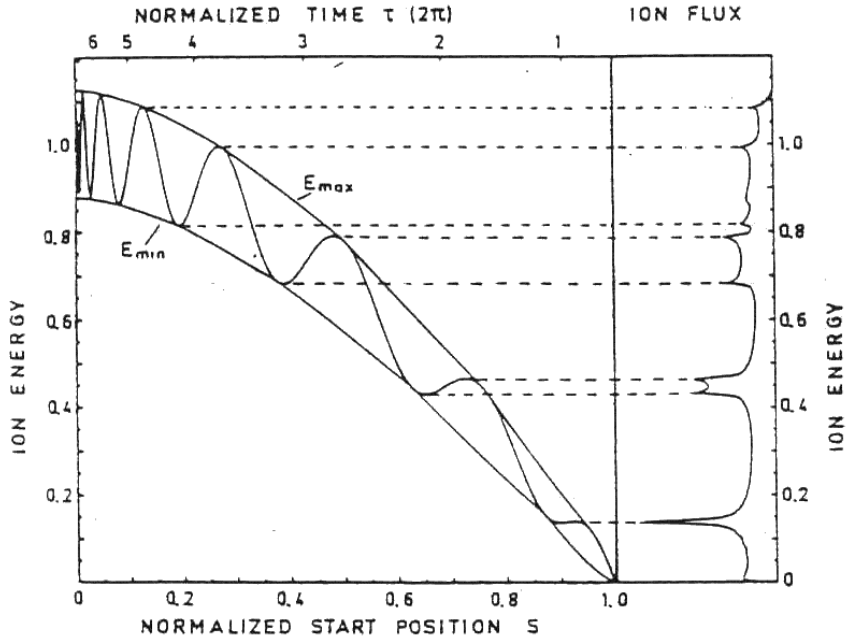

Fig.6.10. Ion energy at the cathode generated from ions in an RF modulated sheath as a function of normalised start position, *S*, (*S* = 0 at the plane of origin and *S* = 1 at the cathode). The vertical diagram on the right shows the resulting IED with the positions of the secondary peaks being related to the modulation of the sheath thickness at the start position, *S* (after ref.[126]).

Turning to the IADs for pressures of 1 and 100 mTorr which are shown in fig.6.8a and b, we find that in contrast to the IADs obtained by scattering alone, these IADs still exhibit near normal angles of incidence even at a pressure of 100 mTorr. This is because the initial ion velocity components were chosen such that the newly-created ion was in thermal equilibrium

with the bulk gas. Hence initially the x, y and z velocity components were very small. Since only the x-component of velocity was affected by the sheath potential and rapidly became very large while the y and z components remained unchanged, the IADs resemble those seen for low pressure plasmas (see fig.5.4, for example). Only at pressures of 100 mTorr and above, where ion impact energies are small, do the initially small y and z velocity components make a noticeable difference to the IAD, skewing the distribution to lower angles by only about 3°.

The conclusions are that charge exchange effects reduce ion impact energies but do not deflect trajectories significantly away from normal incidence.

6.5 Combined Effects of Charge Exchange and Scattering Upon IEDs and IADs

Both collision processes will now be included in the model in order to examine the combined effects of scattering and charge exchange upon IEDs and IADs. Fig.6.11(a-f) show the IEDs calculated with both collisional processes included. As expected, these IEDs show a combination of both of the effects outlined in sections 6.3 and 6.4. As the pressure increases, scattering smears out the IEDs to lower energies, whilst charge exchange produces secondary peaks. Combining both of these effects causes the IED to rapidly lose its form as the pressure rises, until by 30 mTorr the distribution appears very irregular with only a few secondary peaks discernible against the background. At pressures greater than this the whole IED shifts to lower energies and most of the peaks are lost in the background, indicating that the ions lose all ‘memory’ of their initial trajectories due to collisional processes.

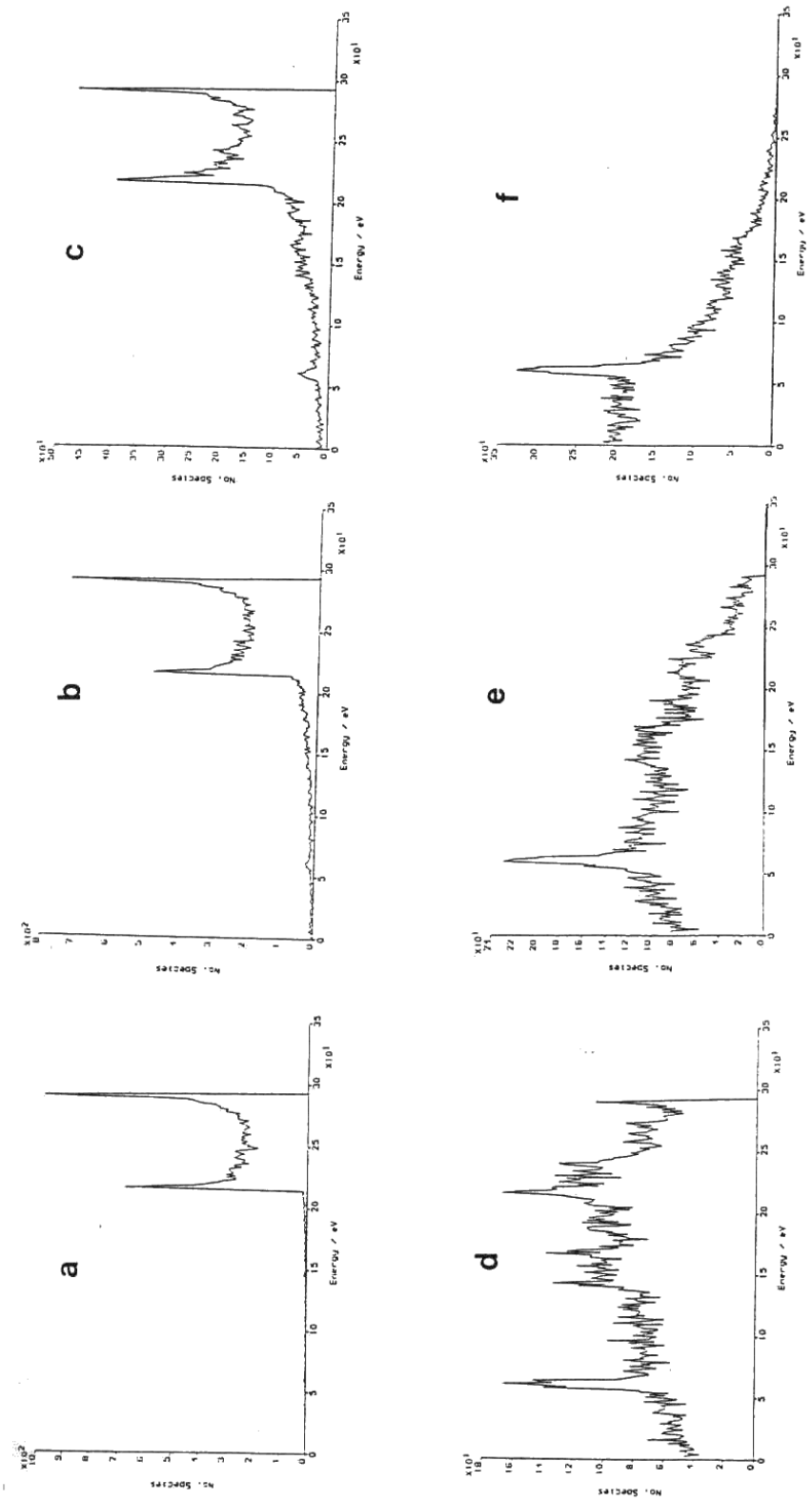
a
b
c
d
e
f
No. Species
Energy / eV

Fig.6.11. IEDs calculated using the standard high pressure plasma conditions incorporating both charge exchange and scattering collisions, for pressures of (a) 1, (b) 5, (c) 10, (d) 30, (e) 50 and (f) 100 mTorr.

The IADs corresponding to the same plasma conditions at pressures of 1 and 100 mTorr are given in fig.6.12a and b. These IADs also show a combination of two effects; the large majority of ions still strike at near normal incidence due to charge exchange, but at higher pressures a tail caused by scattering is seen extending down to angles of about 70°.

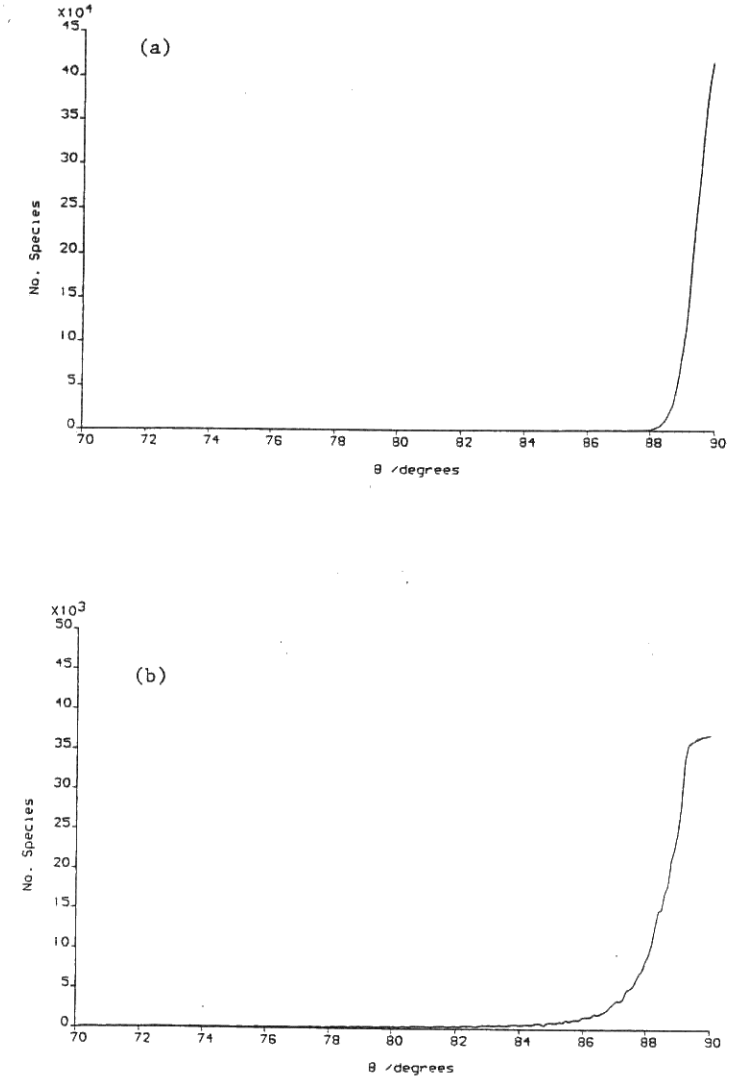

Fig.6.12. IADs corresponding to the conditions of fig.6.11, except at pressures of (a) 1 and (b) 100 mTorr.

The implications of these results for plasma etching are considerable. Firstly, it can be seen that even at fairly low pressures by RIE standards (30 mTorr) about half of the ions strike the electrode at lower energies than in the collisionless case, and with glancing angles. These ions may easily produce mask undercut, so affecting the etch profile. For the standard process

conditions, at pressures between about 20 and 50 mTorr, ions can strike the electrode with almost any energy between 0 and E_2 eV (see fig.5.3), where E_2 is calculated from Equation (5.33). Hence, a crude approximation for an IED under these conditions is a linear distribution between 0 and E_2. At higher pressures ($p \sim 100$ mTorr), the distribution resembles an exponential decay.

It is the ratio of λ_0 to l_{max} that determines which type of IED is seen. This crude way of approximating high pressure IEDs might be useful for plasma process engineers, so a rough guide-line is shown in table 6.2. This is, of course, only valid for Ar plasmas, since more complex gases have not yet been modelled.

λ_0 / l_{max}	**IED Description**
7.0	Well defined IED between E_1 and E_2.
1.4	Well defined IED between E_1 and E_2, with a small tail to low energies.
0.71	
0.35	
0.24	Roughly linear distribution of energies between 0 and E_2.
0.14	
0.07	Exponential-like decay down to E_2.
< 0.05	Exponential-like decay down to $E < E_2$.

Table 6.2. Description of high pressure IEDs. E_1 and E_2 are defined in section 5.2.2.

6.6 Variation of High Pressure IEDs with Frequency

Fig.6.13(A-E) show the effects upon the IED of varying the frequency from 100 kHz to 50 MHz. At low frequencies, secondary peaks do not appear and the IEDs appear similar to low pressure IEDs, except that more ions are scattered to lower energies. Secondary peaks are not seen because the frequency is so low that new ions created in the sheath by charge exchange processes do not experience any modulation of the sheath potential before striking the electrode. As the frequency is increased, the peak separation of the main distribution decreases as described in section 5.3.6. Only when the plasma enters the high frequency regime do secondary peaks begin to appear. The number of these secondary peaks depends upon the frequency of the RF, with more secondaries appearing at higher frequency.

By contrast, IADs show very little variation with frequency, with all the IADs corresponding to the IEDs in fig. 6.13(A-E) resembling fig.6.8b.

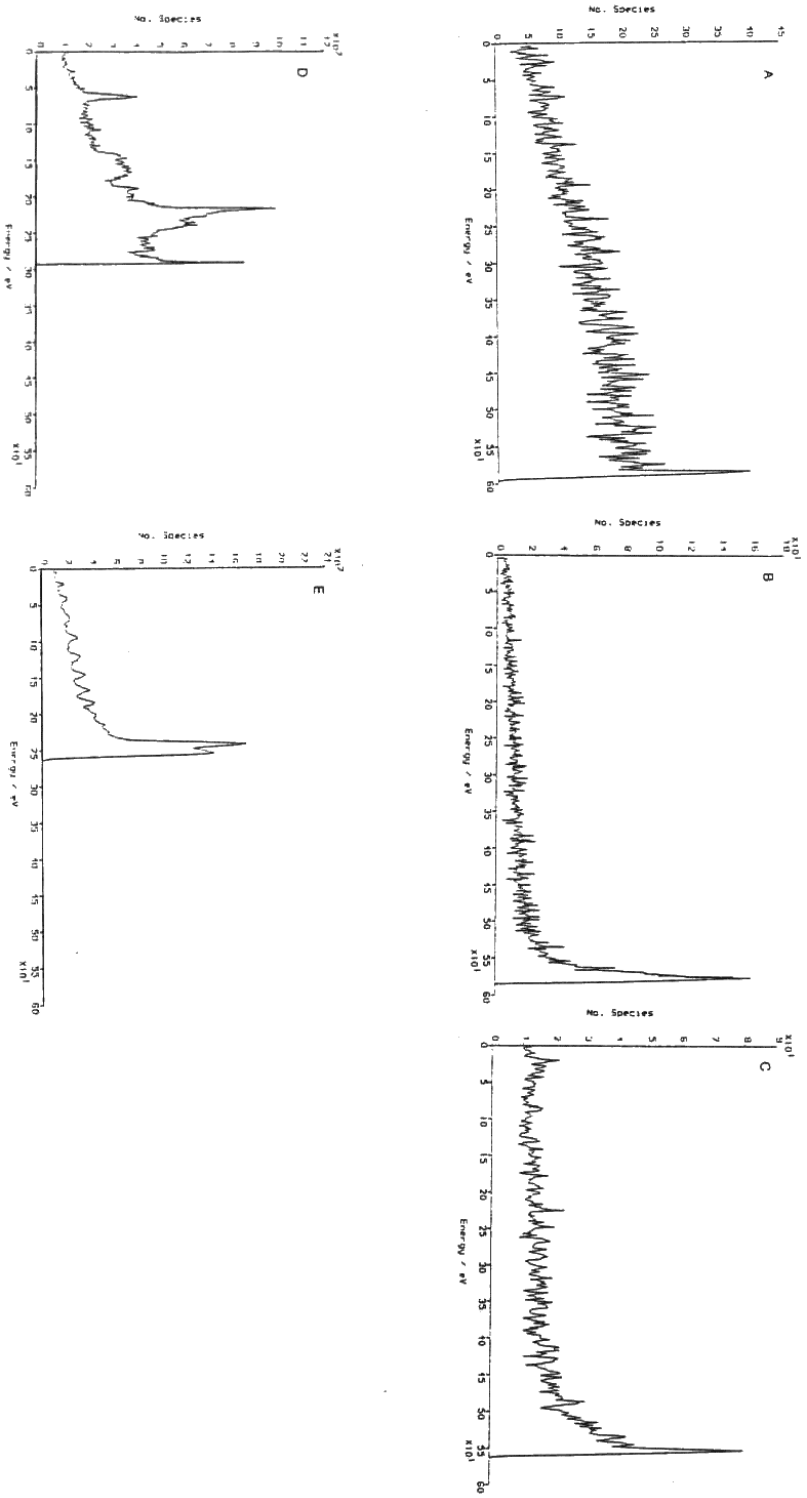

Fig.6.13. IEDs for the standard high pressure plasma conditions at frequencies of (A) 100 kHz, (B) 500 kHz, (C) 1 MHz, (D) 13.56 MHz and (E) 50 MHz.

6.7 Variation of High Pressure IEDs with RF Voltage

The main effect of increasing V_0 upon high pressure IEDs is to spread out the IED to higher energies. Just as the value of $\langle E \rangle$ is proportional to V_0, so the energies of all secondary distributions created by charge exchange will also be proportional to V_0. Fig.6.14a and b show IEDs for $V_0 = 100$ V and $V_0 = 500$ V illustrating this effect. For the 100 V case, the secondary peaks all occur within a small energy range between 0 and 70 eV, and so are difficult to identify. At $V_0 = 500$ V the distribution is well spread out, with all secondary peaks resolved (although the limitation of the number of trajectories still imposes some degree of noise upon the IED). In other words, increasing V_0 increases the dispersion of the IED.

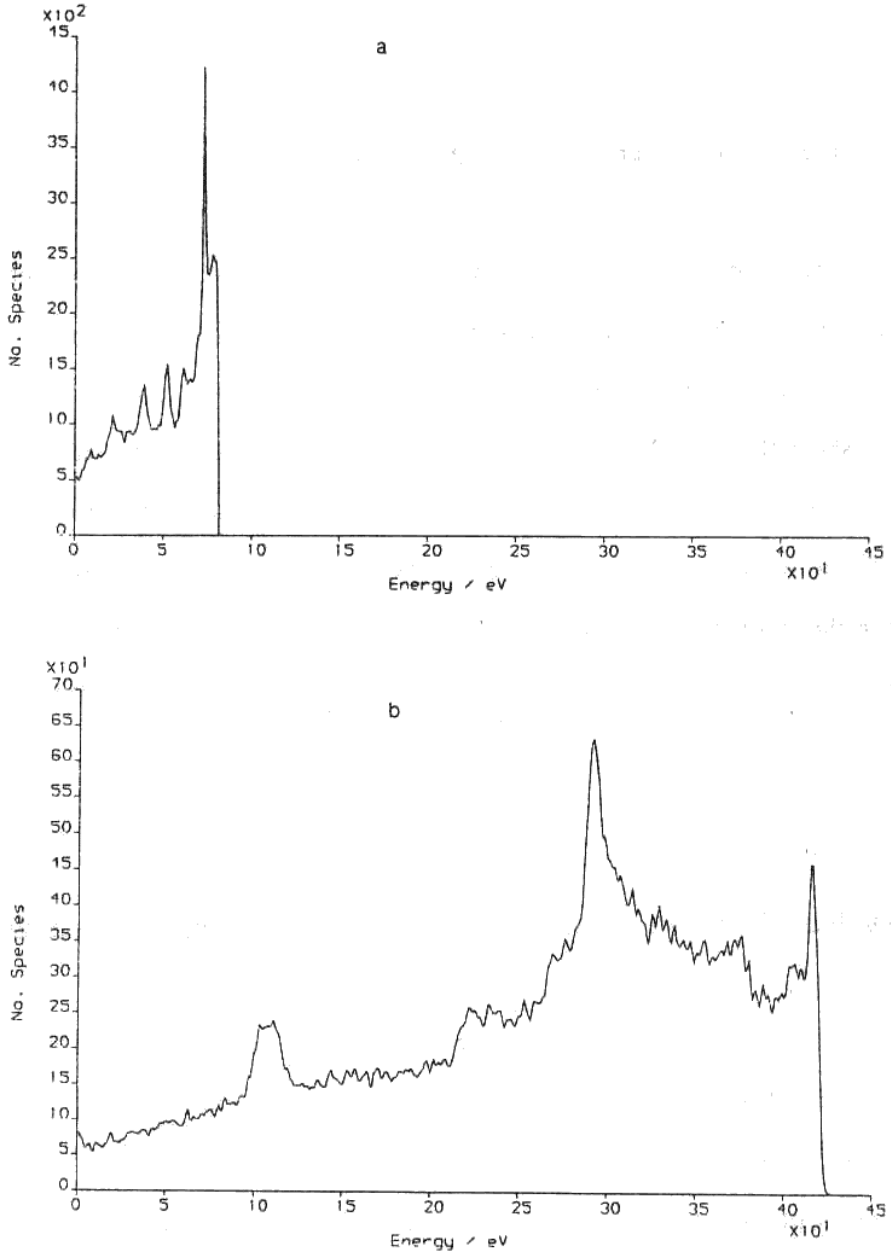

Fig.6.14. IEDs for the standard high pressure plasma conditions at RF voltages, V_0, of (a) 100 V and (b) 500 V.

6.8 Comparison of Simulated High Pressure IEDs with Experimental Observations

As with low pressure IEDs, a scarcity of high resolution experimental observations of high pressure IEDs has been a hindrance to developing more accurate models of the dynamics of ions within RF sheaths. Of the few high pressure IEDs published [122,124-127,134], two have been selected with which to test the theoretical predictions of the model outlined in this thesis. The

first of these is by Kuypers [134] who used the same experimental arrangement described in section 5.4 with which he obtained low pressure IEDs, to measure an IED for an Ar plasma at a quoted pressure of 39 mTorr. Kuypers' IED is shown in fig.6.15a. The main IED shows a tail extending down to low energies with several secondary peaks also appearing. Fig.6.15b shows a simulated IED using the standard values for the plasma conditions.

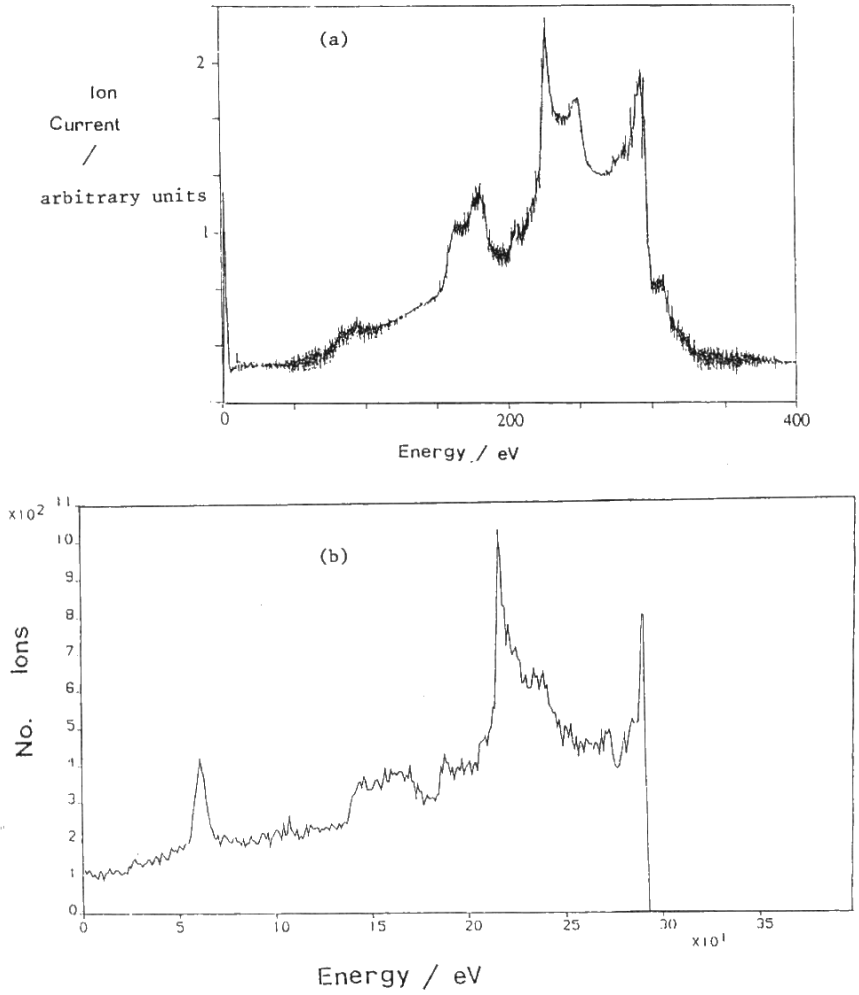

Fig.6.15. (a) Kuypers' [134] experimental Ar^+ IED at a pressure of 39 mTorr.
(b) Simulation of (a) using the standard high pressure plasma conditions.

The values of V_0 and l_{max} for the system were unfortunately not quoted by Kuypers, so they had to be chosen to best fit the observed data. The value of $V_0 = 356$ V (Kuypers states the RF voltage was "between 300 and 400 V") determines the position of the main IED (*i.e.* $\langle E \rangle = 260$ eV), whilst $l_{max} = 4.69$ mm controls the peak separation of $\Delta E = 65$ eV.

The other parameters used were either those quoted by Kuypers (*e.g.* frequency and A_e), or estimated (see section 5.5) to be the standard values (*e.g.* kT_e and kT_i). The value of pressure required in the simulation to reproduce Kuypers' data was 20 mTorr. This is a little odd, since Kuypers quotes a value of 39 mTorr. Assuming for the moment, that the pressure of 39 mTorr is correct, then the values of the collision cross-section for Ar^+/Ar used in the simulation must

include a 50% error. This is not unlikely since cross-sections are difficult parameters for which to obtain accurate absolute values. We noted earlier that other workers have measured values for σ that are much smaller than the ones used in our model, so the absolute value of σ and its variation with energy is still uncertain.

Barring these difficulties, the most striking feature of the simulated IED is how closely it resembles the experimental IED. Not only do all the major peaks have the correct energies, but also all the secondary peak energies have been predicted to within a few eV. The relative intensities of all the peaks are very similar to those seen experimentally, and the overall shape of the two IEDs is almost identical.

There are however, two apparent anomalies. The first is minor and can be explained easily. The experimental IED shows a small shoulder at about 310 eV, which the theory does not predict. Since the peak at 280 eV represents the maximum energy E_2 that an Ar^+ ion can obtain using the present model, this high energy shoulder cannot be due to Ar. It is probably due to the presence of a contaminant (such as O_2 or N_2) in Kuypers' system. Since these gases have a lower mass than Ar, ΔE would be larger and so a small peak would be expected to appear either side of the main distribution. Evidence for slight contamination in Kuypers' system was previously noted in fig.5.35A.

The second anomaly is more difficult to explain. This is the size of the secondary peak at about 65 eV. The simulation predicts this peak to be a sharp spike of roughly equal intensity to the secondary peaks at about 150 eV. In fact, the experimental IED shows this peak as nothing more than a small shoulder on the increasing baseline. There are three possible explanations for this:

(a) The pinhole used to collect ions could be a source of non-uniform fields, which might distort the local sheath potential deflecting ion trajectories away from the opening. High energy ions would pass through almost undeflected, but lower energy ions could be easily deflected away from the detector. Thus, the efficiency of the ion energy analyser would be critically dependent upon the diameter of the pinhole. Circumstantial evidence for this is that apart from the IED in question, Kuypers never presents an IED containing a peak with an energy lower than about 150 eV.

(b) Alternatively, the resolution of parallel plate analysers often depends upon the incident ion energy [167]. It is highly likely that the resolution of Kuypers' detector (which was quoted as about 3 eV), rapidly worsens as the ion energy falls below about 100 eV. This would result in the spreading out of sharp, low energy peaks into broad, diffuse features.

(c) Finally, since Kuypers used a pinhole/detector system to extract ions from the plasma, the pinhole depth would automatically create a preferential angle of acceptance for incoming ions. This angle would be normal to the plane of the electrode, and ions at normal incidence would pass uninhibited through the pinhole to strike the detector. Ions striking the electrode at glancing angles might not be able to reach the detector since they would impinge upon the walls of the pinhole. These low angle (and therefore low energy) ions would be lost as a contribution to the signal at the detector. A simulation of the angles at which ions of energy < 70 eV strike the electrode was performed to verify this hypothesis. It was found that approximately half of these low energy ions strike the electrode at near normal incidence (those caused by charge exchange), whilst half strike at angles between 0° and 80°. This might immediately account for a factor of about 2 in the intensity of observed peaks at low energies.

A combination of all three effects might significantly reduce the intensity of low energy peaks, such as the anomalous 65 eV peak.

The second set of experimental observations to be compared with predictions are data by Sawin *et al* [127]. These workers measured Ar plasma IEDs at the *anode* of a parallel plate reactor at pressures of 10, 50 and 500 mTorr. They then visually estimated the extent of the dark space above the anode for the 3 process pressures, obtaining values of 10, 5 and 4 mm, respectively. They also measured the RF voltage as $V_0 = 65$ V. They then attempted to simulate their IEDs by using a Monte Carlo computer program similar to the one described in the present work. Although their program included both scattering and charge exchange effects, they only used an RF-modulated uniform field model of the sheath to calculate the ion trajectories. The IEDs they observed along with their simulations are shown in fig.6.16.

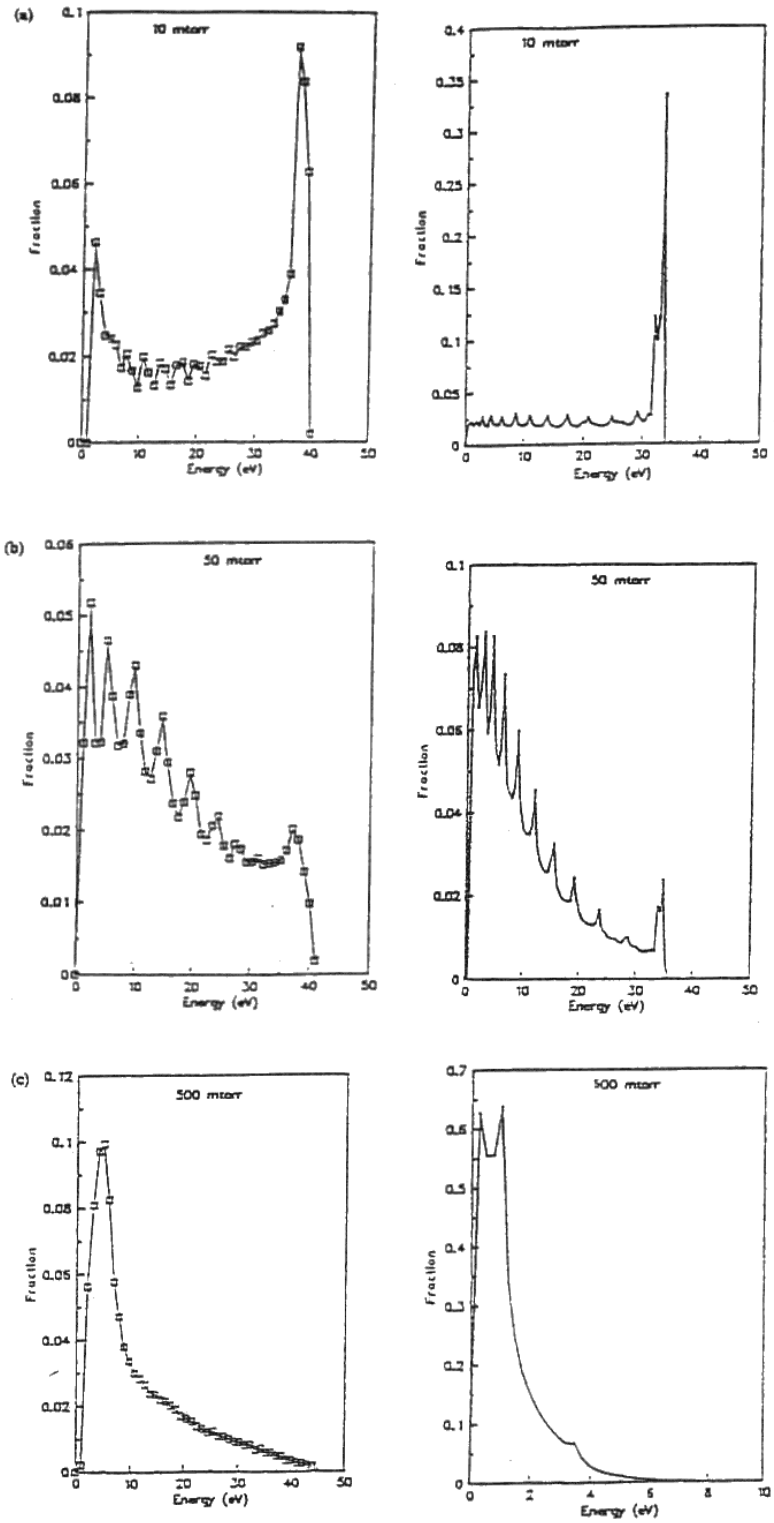

Fig.6.16. Experimental IEDs (left) and theoretical simulations (right) for Ar plasmas at pressures of (a) 10, (b) 50 and (c) 500 mTorr, after Sawin *et al* [127].

The experimental IEDs exhibit several interesting features. Firstly, the secondary peak structure is very well defined for the two lower pressure experiments. At the very high pressure of 500 mTorr however, all secondary peaks have been absorbed into the distribution, which now exhibits an exponential-like decay. Turning to their simulated IEDs, these bear only an overall qualitative resemblance to the observed data, and in fact the high pressure IED simulation is significantly different to the experimental distribution.

Using Sawin *et al*'s quoted plasma conditions, along with estimates for the parameters they did not quote, the experimental IEDs were simulated using the model described in this thesis, with the results being given in fig.6.17. The plasma conditions used for these simulations were: $V_0 = 65$ V, $f = 13.56$ MHz, $A_e = 1.0$, $kT_e = 2.5$ eV, $kT_i = 0.05$ eV and $l_{max} = 10,\ 5,$ and 0.6 mm. The electron and ion temperatures were estimated values. It should be noted that Sawin *et al*'s model does not include any value for the floating potential, V_p^0. It is highly likely (as they note, and has been calculated here), that Vp^0 makes a significant contribution in their plasma system. V_p^0 has been calculated to be about 19 eV, which for these low energy IEDs greatly alters the value of $\langle E \rangle$. Consequently, Sawin *et al*'s simulations predict a value of $\langle E \rangle$ that is much lower than that seen experimentally. This omission has been corrected in our simulations.

We shall now make a detailed comparison of the two simulations and the experimental IED for each of the three pressures studied.

(a) **10 mTorr**: The experimental IED (fig.6.l6a) shows a single peak ($\Delta E = 0$) at $\langle E \rangle = 37$ eV. There is a large tail extending down to low energies, which curiously increases in intensity at very low energies ($E < 5$ eV). This latter point may be due to processes similar to the pinhole distortions and acceptance angle effects described previously. Sawin *et al*'s simulated IED predicts the appearance of a large single peak (although at too low an energy due to V_p^0 not being included in their model), but the relative intensity of the tail is about four times too small. In contrast, turning to fig.6.17A, it can be seen that our simulation accurately reproduces the experimental IED. The resolution of secondary peak detail was limited by computer time and memory, but even so it can be seen that the overall resemblance is remarkably close. The apparent peak at very low energies is not reproduced however, suggesting that this may well be an artifact of the apparatus.

(b) **50 mTorr**: The experimental IED (fig.6.l6b) shows that the main peak at 37 eV is now much reduced in intensity compared to the large background. This background now exhibits many secondary peaks. Sawin *et al*'s simulation is again reasonably similar to the measured IED, but the ratio of the intensities of the main distribution to the background is still incorrect. Fig.6.17B shows the simulation performed using our model. The overall shape of the IED is much more closely predicted, although as before, detail of the secondary peaks could not be resolved due to lack of computing power.

(c) **500 mTorr**: The measured IED (fig.6.16c) shows a gradual decay from an energy value of 5 eV to about 45 eV. There is a sudden drop in intensity at $E < 5$ eV which is unexpected. It is highly likely that this drop is a direct reflection of the decrease in sensitivity of the pinhole/detector system that would be expected from the arguments explained before. Sawin *et al*'s simulation performed very poorly at this pressure. Using their measured value of $l_{max} = 4$ mm they obtained an IED that dropped rapidly to zero intensity by about 5 eV! The first

thought is that there must be something severely wrong with their model. To check this hypothesis, the IED was calculated using our model. Unfortunately, the resulting simulated IED was almost identical to their simulated IED, and both did not resemble the true IED at all. Therefore, either there is something wrong with the description of collisions in both models, or we must look for another explanation.

A pressure of 500 mTorr is very close to the limits for which the models described in this thesis are valid. For higher pressures, and hence lower energy collisions, any approximations made about the description of the collision dynamics may become significant. In particular, a hard-sphere model is known to be a reasonable approximation to atomic collision dynamics at high impact energies [189]. However, as the energy decreases, the detailed form of the interaction potential becomes increasingly more significant, and the hard-sphere approximation becomes less valid. At very low energies, orbiting and *rainbow* effects, and even quantum phenomena become important. Therefore, one explanation of why the models do not predict the 500 mTorr IED very well is that the descriptions of low energy collision processes are not precise enough. If this were true, it would limit the use of the present model to pressures where collision energies are high enough for the inherent approximations to be acceptable. This upper limit is estimated to be about 100 mTorr, or $\lambda_0 / l_{max} = 0.08$.

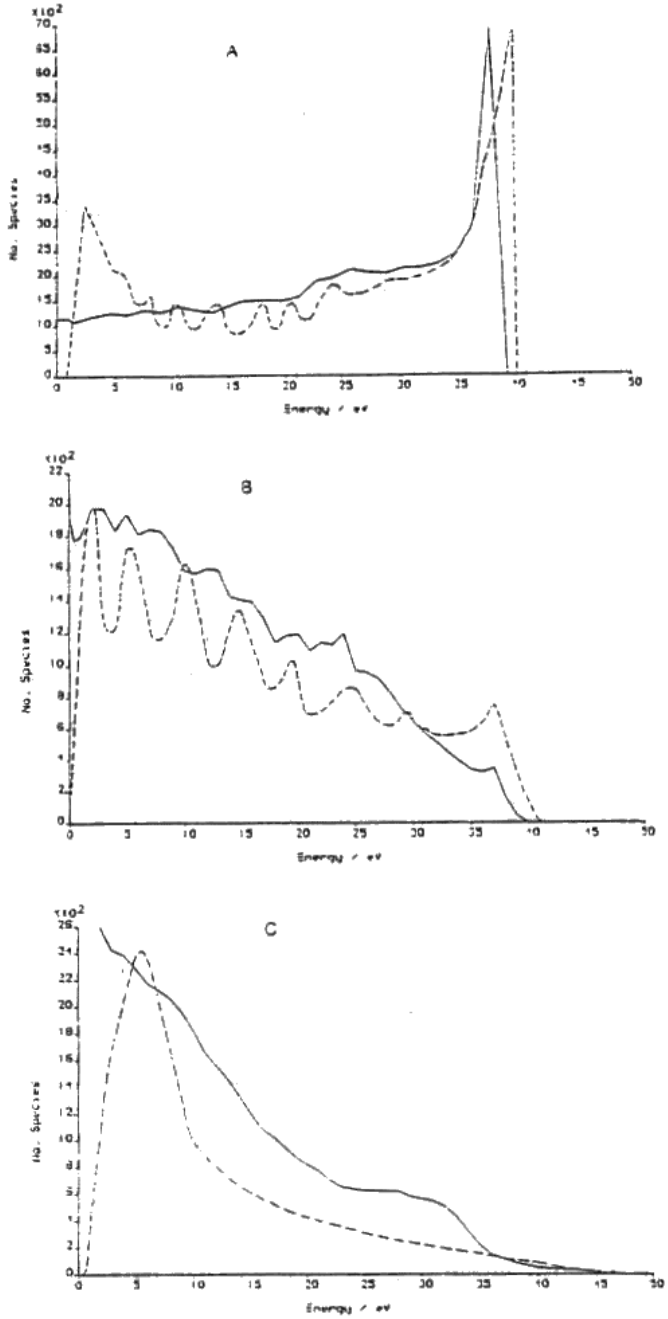

Fig.6.17. Experimental [127] IEDs (dashed lines) and simulated IEDs (full lines, this work) for Ar plasmas at different pressures. Only 5×10^4 ions were used in the simulations, so secondary peak detail has not been resolved. Plasma conditions were as quoted by ref.[127]; V_0 = 65 V, A_e = 1.0, kT_e = 2.5 eV, kT_i = 0.05 eV and f = 13.56 MHz. (A) 10 mTorr, l_{max} = 10 mm, (B) 50 mTorr, l_{max} = 5 mm, and (C) 500 mTorr, l_{max} = 0.6 mm and kT_e = 2 eV. For (C), l_{max} was chosen to fit the data rather than use the measured value of 4 mm.

However, there may be an alternative explanation. Looking at fig.6.16c, it is interesting to note that even at 500 mTorr some ions still strike the electrode at energies > 40 eV. The only way ions could have achieved such high energies in that system is if they have experienced the full sheath potential. A quick calculation shows this to be very strange indeed. Using Equation (6.24), the mean free path of an Ar^+ ion at 500 mTorr is about 6.6 μm. From Equation (6.25), the probability that an ion could travel a distance of $l_{max} = 4$ mm without undergoing a single collision is ~ 10^{-22}. Yet the experimental IED shows a significant number of ions with these high energies.

One possible explanation is that the sheath thickness was actually much smaller than that quoted by Sawin *et al*. If a fitted value of $l_{max} = 0.6$ mm is used, we obtain the simulated IED shown in fig.6.17C, which although not an exact prediction of the observed IED, does provide a much more accurate representation than the ones obtained using the previous value $l_{max} = 4$ mm. This simulation even exhibits the slight increase in E_2 (from 40 eV at $p = 10$ mTorr to 47 eV at $p = 500$ mTorr) seen experimentally. However, it is still unclear why the 'measured' value of l_{max} should be ~10 times greater than the value needed to fit the IED theoretically. This is discussed further in section 6.9.

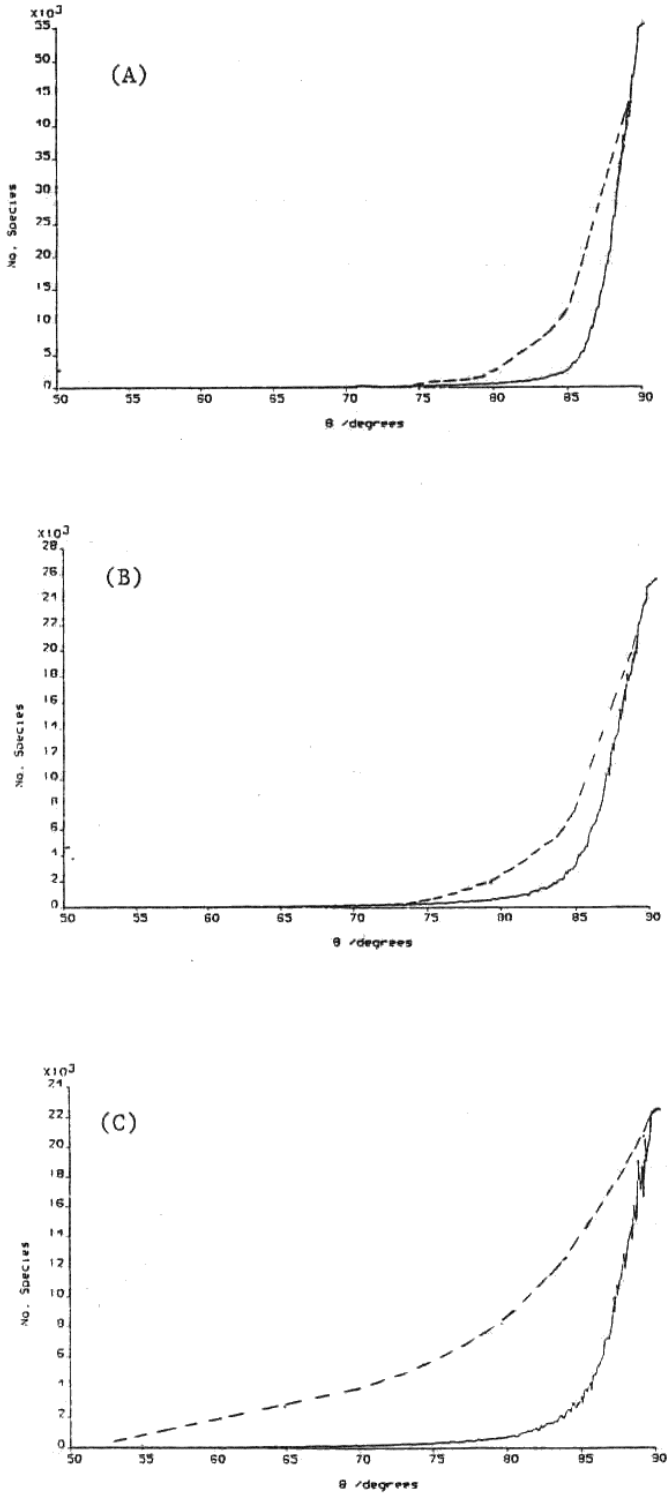

Fig.6.18. Experimental [127] IADs (dashed lines) and our simulated IADs (full lines) for the same Ar plasma conditions as fig.6.17. The data of ref.[127] have been replotted on our scale of θ for ease of comparison.

The detector used in the experiments was a segmented retarding field analyser (RFA) which enabled IADs as well as IEDs to be measured (see fig.1.19.2). The angular resolution was about 3° and only angles of $\theta > 50°$ were presented.

Fig.6.18 shows the experimental IADs for the 3 pressures, along with IADs calculated using our model. It can be seen that for pressures ≤50 mTorr the simulated IADs are reasonably accurate. The 500 mTorr IAD (calculated using lmax = 0.6 mm) is however, markedly different to the observed distribution. The reason for this is still unclear. The shape of the observed 500 mTorr IAD suggests that very few ions are striking the electrode at near normal incidence, with a large proportion of ions being scattered into shallower trajectories. This would seem to indicate that charge exchange processes were not occurring to any great extent in this plasma. If the 500 mTorr IAD is simulated using a model for collisions that includes *only* scattering (see section 6.3), we obtain a much closer fit to the experimental IAD.

One theory therefore, is that the cross-sections for charge exchange and scattering do not follow an extrapolation of the curves shown in fig.6.3 at energies < 1 eV, but rapidly drop to zero. This would increase the mean free path for low energy ions by a large factor, which is equivalent in our model to using a smaller value for the sheath thickness parameter. If $\sigma_e(E)$ decreases faster than $\sigma_s(E)$, then collisions would become predominantly scattering rather than charge exchange, leading to the broad IAD seen in fig.6.18C. Unfortunately, there is virtually no experimental evidence to confirm this hypothesis, and so it must remain speculative. Measurements of $\sigma_e(E)$ for Ar^+/Ar by 11 independent workers are listed in ref.[189]; none give values of a for collision energies less than about 5 eV. The experiment at the lowest energy was performed by Dalgano [192,195] who obtained a value of $\sigma_e(\sim 5 \text{ eV}) \sim 62$ Å^2 with the curve of $\sigma_e(E)$ exhibiting a steady increase as E decreased. Moreover, the theoretical predictions of the value of $\sigma_e(E)$ calculated using the Firsov formula [193,194] do not predict any sudden drop in cross section as E approaches zero. Since for Ar, resonant charge exchange is likely to be the dominant process [189], we would expect $\sigma_e(E)$ to increase monatonically as E decreases.

Further evidence against the hypothesis that $\sigma_e(E) \to 0$ as $E \to 0$ is given in table 6.3. This shows the mean energy of collisions calculated for the plasma conditions used to simulate Sawin *et al*'s IEDs. As expected, at lower pressures ions travel further and obtain more kinetic energy before undergoing a collision. However, even at 500 mTorr ions generally still collide with energies greater than thermal. In other words, the collision energy still just has a value where $\sigma_e(E)$ can be interpolated directly from fig.6.3. This would seem to effectively rule out the hypothesis mentioned above being a reason for the discrepancy between theoretical predictions and simulations of IEDs at very high pressures. This hypothesis is therefore abandoned. An alternative theory is presented in the next section.

Pressure / mTorr	Mean collision energy / eV	Mean free path / mm
1	18	33.6
10	12	3.36
50	9	0.67
100	8	0.34
250	6	0.13
500	4.5	0.067
1000	2.7	0.033

Table 6.3. Mean Ar^+/Ar collision energy and mean free path at different pressures in an RF sheath for the conditions of Sawin *et al*'s [127] calculated IEDs.

6.9 Estimation of l_{max}

We have seen that the 500 mTorr IED obtained by Sawin *et al* [127] can be simulated if a value of l_{max} ~ 0.6 mm is used, rather than the measured value of 4 mm. This measured sheath thickness was obtained by visual inspection of the extent of the dark space, but the exact experimental procedure for doing this was not detailed in their paper. They claim an accuracy of ±0.5 mm for their measurements, and this would clearly not explain the factor of 10 decrease in sheath thickness required by our simulation. One possibility is that the electrical sheath and the dark space thicknesses are not synonymous. The dark space may only be a secondary effect associated with the sheath, but not exactly mirror its dimensions.

Moreover we should ask the question: 'What actually do we mean by the sheath boundary?'. The computer model assumes this boundary is a sharp interface defined by the plane of origin. However the exact plane of origin will be different for electrons of different energies (see section 7.2.6). Also, for a quarter to a half of the RF cycle the sheath thickness will be at its minimum. Since electrons travel in general about 10 times faster than a typical 13.56 MHz sheath boundary, given a correct input phase, electrons can travel nearly all the way from the plane of origin to the cathode exciting $Ar \rightarrow Ar^*$ en route. Therefore, we should expect that the sheath would only be *dark* for the portions of the cycle where the potential is greater than its minimum value. It seems that at best, an optical judgement of the width of the dark space might only give a time-averaged value for the sheath thickness, rather than the maximum value.

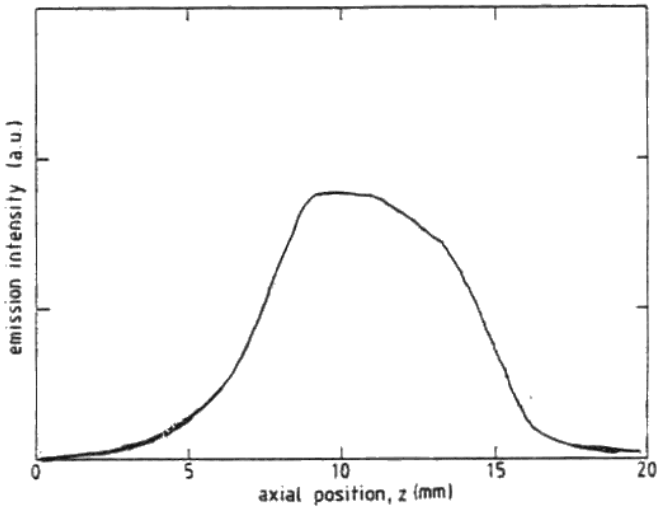

Fig.6.19. The spatial variation in emission intensity from a 50 mTorr Ar discharge. The cathode is at $z = 0$ and the anode at $z = 20$ mm (adapted from Bisschops, ref.[122]), a.u. = arbitrary units.

Several workers have studied the dark space region using different methods. Fig.6.19 shows the spatial variation of Ar^* emission intensity between the electrodes of an RF reactor at about 50 mTorr obtained by Bisschops [122]. The observed emission clearly does not end abruptly, but decays away over the space of a few mm. This makes measurement of the width of the dark space very difficult and open to subjective judgement.

The exact width of the dark space will depend upon the definition of where the boundary lies. For the purposes of the comparison of various workers' measurements, we redefine the dark space boundary as that position at which the emission intensity drops to a half of its value in the centre of the discharge. For Bisschops' data therefore, the dark space is about 5 mm from either electrode. Bisschops also presents data which shows that at higher pressures the dark space region decreases in size, with the intensity distribution between the electrodes becoming non-uniform. He explains this non-uniformity as being a result of extra excitation due to secondary electron emission from the cathode (see section 7.3). Such secondary electron effects can further confuse measurements of the dark space.

Spatially resolved optical emission studies for other systems [197] also show a gradual (rather than an abrupt) decrease in emission intensity near the electrodes, leading to uncertain measurements of the dark space region.

Langmuir probe studies have been performed in which the electron density has been measured as a function of distance from the electrode [134,198]. These studies show the same sort of gradual decrease in electron density near an electrode. If we assume that most Ar excitation is caused by electron impact, then the electron density at any point in the plasma determines the number of excitation reactions occurring, and hence the brightness of the plasma at that point. Therefore, probe results also indicate that a better picture for the dark space is a diffuse region with no clear boundary.

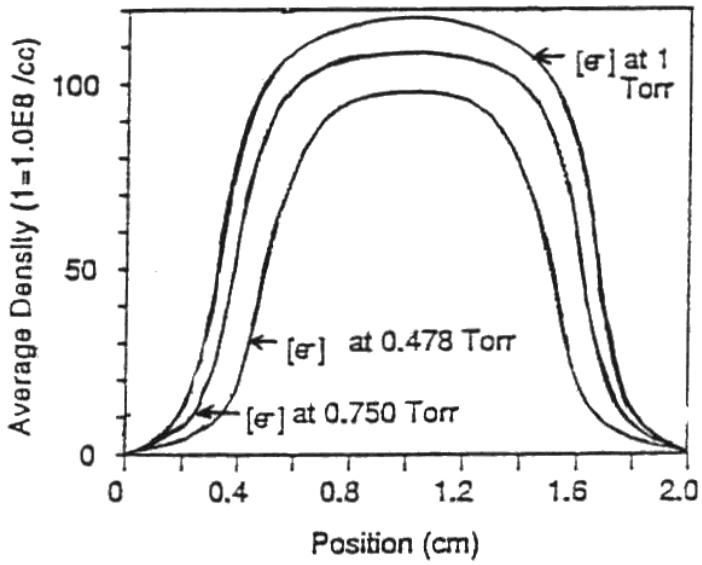

Fig.6.20. Average electron density calculated for an Ar discharge between the cathode (0 cm) and anode (2 cm) of a 13.56 MHz reactor (adapted from ref.[196]).

Theoretical studies corroborate these findings. Sawin and Goglides [196] and Gill [142] have both used models of the plasma/sheath boundary to calculate the electron density as a function of distance from the electrode for different pressures. Fig.6.20 show the results of Sawin and Goglides' calculations. As the pressure increases, the region of low electron density moves closer to the electrode (*i.e.* the dark space shrinks).

Typically, the uncertainty in the position of the dark space boundary increases with pressure. In general, at low pressures (< 50 mTorr) we get a large, sharply-defined dark space/plasma boundary. As the pressure is raised, the dark space decreases and becomes more diffuse. Fig.6.21 is an exaggerated illustration of this effect. It can be seen from this diagram that at low pressures the extent of the dark space is relatively easy to estimate, and moreover, yields a reasonably accurate value for the electrical sheath width. At higher pressures the plasma region is dimmer and so the dark space is no longer significantly darker than the plasma. Also, the boundary is now more diffuse and so its position is very difficult to estimate. If the 50% intensity criterion is adopted, it is clear that the resulting value for the dark space will be a gross over-estimate of the true electrical sheath width. Accordingly, we may require a more accurate method to determine the electrical sheath width for the higher plasma pressures.

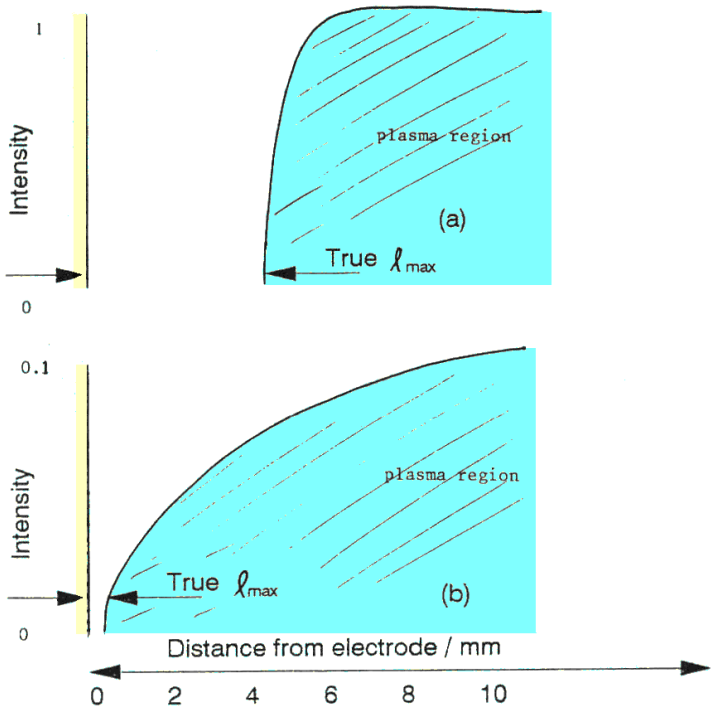

Fig.6.21. Proposed description of the emission intensity of Ar (in arbitrary units) near an electrode for (a) low pressures, say 10 mTorr, and (b) high pressures, say 500 mTorr. This is very exaggerated, but it serves to show how at low pressures the dark space may be accurately estimated as the electrical sheath thickness, whereas at high pressures one obtains a gross over-estimate.

An important contribution has been made by Morgan [199], who has derived a formula for the sheath thickness in high pressure RF systems. Morgan's theory is based upon standard expressions for the space-charge limited current through a sheath derived using Poisson's Equation (1.5.7). He makes the assumptions that:

(i) Whenever an ion in the sheath undergoes a collision, it starts again from rest. In other words the theory incorporates only charge exchange effects.
(ii) The stationary ion then undergoes uniform acceleration.
(iii) The electric field in the sheath is constant over the last mean free path of the ion before it strikes the electrode.
(iv) The current density is assumed to be constant, *i.e.* independent of V_0.

The expression given by Morgan relates l_{max} to the ionic mean free path λ_0 and maximum sheath potential through

$$l_{max} = 4.93\times10^{-5}\ (\tfrac{1}{2}\, e\, \lambda_0 / m_i)^{1/5}\ (V_{pe,max})^{3/5} \qquad (6.37)$$

where $V_{pe,max}$ is the maximum sheath potential which is calculated using Equations (5.13) and (5.15) for the cathode and anode, respectively. The assumptions used to derive Equation (6.37)

are a very primitive description of the behaviour of ions within the sheath. Therefore, Equation (6.37) should be treated with caution. This expression was rewritten in the form

$$l_{max} = 4.93\times10^{-5} \{½\, e / (3.5\times10^{19}\, p\, m_i\, \sigma_{max})\}^{1/5}\, (V_{pe,max})^{3/5} \qquad (6.38)$$

where p is the pressure in mTorr and σ_{max} is the maximum total collision cross section (~ 86 Å^2). Equation (6.38) shows that ~max is proportional to $p^{-1/5}$, so that at pressures of greater than about 20 mTorr, l_{max} is very insensitive to pressure and should remain almost constant.

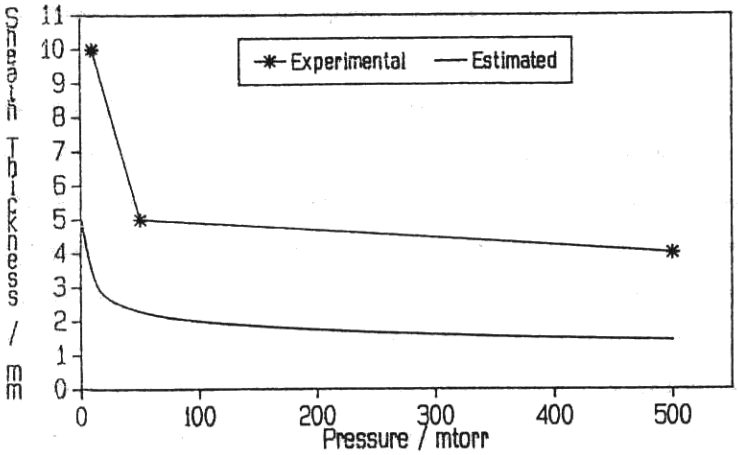

Fig.6.22. Sheath thickness versus pressure for Sawin *et al*'s experimental observations [127] and the predictions of Morgan's Equation (6.38).

The predictions of this expression are plotted in fig.6.22 along with the experimental values observed by Sawin *et al*. It can be seen that Equation (6.38) predicts values of l_{max} that are much smaller than those observed. The expression predicts a value for l_{max} at 500 mTorr of 1.42 mm, which is only a factor of 2 away from the value of 0.6 mm required by our IED simulation.

Using Morgan's expression for the previously presented simulated data of Kuypers' IEDs, along with a value of $V_{pe,max}$ = 577.6 V, we obtain l_{max} ~ 10 mm (for p = 20 mTorr) compared to the required value for accurate IED simulation of 4.69 mm. Again, the formula predicts a value that is about 2 times too large. Also, the simulations of Bisschops' measured IEDs presented in section 5.9.2 required a value of l_{max} = 1.40 mm. Morgan's formula (using p = 100 mTorr and $V_{pe,max}$ = 161.9 V) gives l_{max} = 3.45 mm, again a little over twice the required value.

Equation (6.38) was originally derived by Morgan using a value for the leading constant (4.93×10^{-5}) which assumed a constant current density in the sheath region, having a value appropriate to Morgan's plasma system. In other words, this leading constant is a fitting parameter optimised for Morgan's reactor. In order to make Equation (6.38) more suitable for general use, the leading constant may be modified to give a value more representative of typical plasma processes. By comparison with the 3 plasma systems mentioned above (Kuypers, Sawin *et al* and Bisschops), we found that this leading constant should be multiplied by a correction factor of 0.4-0.5, having an average value of 0.43. Hence, the modified version of Morgan's equation using this empirical correction factor is

$$l_{max} = 2.12\times10^{-5} \{½\, e / (3.5\times10^{19}\, p\, m_i\, \sigma_{max})\}^{1/5}\, (V_{pe,max})^{3/5} \qquad (6.39)$$

Until a better method is produced, the value of l_{max} required to simulate high pressure IEDs is probably best calculated using Equation (6.39). The errors produced when using this expression are likely to be much less than those incurred by estimating l_{max} from the visual extent of the dark space. Care must be taken when using Equation (6.39) for low pressure plasmas (*i.e.* $l_{max} << \lambda_0$), since many of the assumptions used in its derivation will be untrue under these conditions. The range of plasma conditions for which Equation (6.39) is valid can only be obtained by performing many more comparisons between experimental and calculated IEDs in different etch systems.

6.10 Neutral Particle Energy Distributions

The model of ion collisions within the sheath that has been presented above considers only ion trajectories. However, the atoms and neutral species that are struck by energetic ions will themselves obtain a significant fraction of the ion kinetic energy. These neutrals will recoil with high velocity and may strike the electrode surface with high energies, initiating etch mechanisms. Consequently, in order to understand the nature of the energetic particles striking the substrate surface, we need to study not only IEDs and IADs, but also neutral particle energy distributions (NEDs) and angular distributions (NADs).

There are essentially two independent origins for fast neutrals: namely those formed by the two types of collisional processes, charge exchange and scattering. These shall be considered separately:

(a) Charge Exchange

Since in charge exchange, no momentum is transferred from the ion to the atom, after the interaction has occurred we are left with a new ion created from an initially thermal atom and a fast neutral moving along the same trajectory as the original ion (see section 6.2.3). Thus, fast neutrals created in this process will simply have the pre-collision velocity components of the initial ion. Since ion trajectories are predominantly normal to the electrode, fast neutrals created by charge exchange will also exhibit near normal trajectories. These neutrals will obviously not be affected by the sheath potential and so will continue towards the electrode until they strike an obstruction (the electrode itself or another gas particle).

(b) Scattering

For scattering collisions, both momentum and energy are exchanged between the colliding species. The equations governing this process (assuming hard sphere dynamics) have been given previously in section 6.2.1. It was shown in Equation (6.5) that for the case of species of equal masses colliding (as in Ar plasmas), the atom would recoil with a velocity v_2 at an angle β (where $\beta = 90° - \gamma$). The method for choosing γ was detailed in section 6.2.2 along with the method to convert the post-collision velocity components to the frame of reference relative to the electrode. By use of these same methods, we can calculate the trajectory of the neutral species immediately following the collision.

Fast neutrals created in either process (a) or (b) are assumed to follow a straight line path until they suffer one of four possible fates

(i) The neutral strikes the electrode. Its energy and impact angle are then stored to contribute to the NED and NAD, respectively. The program then loops back to choose a new ion.

(ii) The neutral collides with another species. Since for Ar plasmas the concentration of Ar atoms is much greater than for any other type of species, it will be assumed that this collision will be a neutral-neutral scattering process. Charge exchange will not occur since neither species is ionised. The original fast neutral will therefore transfer some of its energy and momentum to its collision partner, and both will recoil.

(iii) If the velocity components are such that the neutral is travelling away from the electrode (*i.e.* $v_x < 0$), it is possible for it to pass through the plane of origin to enter the plasma region. These neutrals that leave the sheath will be termed *backscattered neutrals*, and their subsequent trajectories are ignored.

(iv) The energy a neutral obtains in a collision may be very small. Such neutrals may have kinetic temperatures only just above the bulk equilibrium temperature. A parameter, E_{therm} is defined as the energy below which a neutral is considered to have reached thermal equilibrium with the bulk gas. Such slow neutrals are no longer worth following, since they will not be significantly different to the majority of the plasma species.

6.11 Calculation of Neutral Atom Cascades

In order to calculate the possible fates of a fast neutral, it is necessary to know the mean free path of the neutral at the plasma pressure. The cross section, σ, for elastic hard-sphere collisions of Ar atoms is 41.62 Å^2 [189]. The expression for the mean free path for Ar atoms averaged over all velocities, $\bar{\lambda}_0$, is the same as that for Ar^+ ions and has been given previously in Equation (6.23). This mean free path will be energy dependent, since we know that at the limit of a fast species colliding with a stationary one we obtain Equation (6.24). From ref.[209], the true mean free path λ_v of an atom of mass m with velocity v is given by

$$\lambda_v = mv^2 \sqrt{\pi} / \{ 2n\sigma \psi(v/v_0) \} \qquad (6.40)$$

where

$$v_0 = (2kT / m)^{1/2} \qquad (6.41)$$

and

$$\psi(x) = x \exp(-x^2) + (2x^2 + 1) \int_0^x \exp(-y^2).dy \qquad (6.42)$$

Using these expressions, the value of the mean free path for an atom having velocity v is given in fig.6.23. It can be seen that λ_v rises from a value of 0 at $v = 0$ to a value $\sqrt{2}$ times the expected mean free path calculated from Equation (6.23) when the velocity is large. This curve was fitted by simple linear interpolation between 10 data points situated along the curve. In this way, the mean free path for an atom having any velocity may rapidly be calculated. The distance to the

next collision was then calculated using the Monte Carlo techniques described in section 6.2.4.

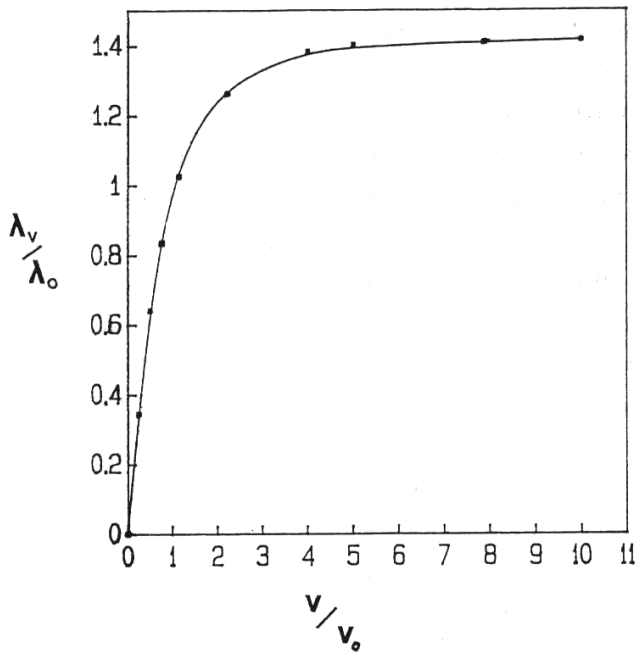

Fig.6.23. The ratio of the mean free path λ_v at velocity v to that averaged over all velocities λ_0, where v_0 is the average velocity calculated from Equation (6.41), as a function of velocity.

In order to obtain accurate NEDs, the trajectory of every atom that undergoes a collision with a fast species must be followed. The procedure adopted is to calculate Ar^+ trajectories until a collision occurs. The type of collision (scattering or charge exchange) is then determined (see section 6.2.5) and the post-collision ion and atom trajectories are calculated. Four pieces of information about the atom (x,y,z velocity components and distance from the electrode) are then saved in an *array* in the computer memory. This '*atom array*' contains data on all the atoms that have undergone collisions and whose trajectories are yet to be followed. The ion trajectory is continued until it completes its journey to the electrode, with any other atom collision data occurring en route being added to the array.

The array is then examined. If it is empty a new ion is chosen starting at the plane of origin, and the process repeated until all the ions have been processed. If the array is not empty however, the details of the last atom are recalled from the array and the subsequent post-collision trajectory of the atom is followed. If this primary atom undergoes a collision with another atom, the details of the second atom are saved into the array as before.

The primary atom is followed until it suffers one of the fates mentioned above. If the atom strikes the electrode, its energy and impact angle contribute to the NED and NAD, and the details of the next atom are recalled from the array for processing. If the atom backscatters into the plasma region, it is considered lost (although these data are discussed in section 6.15), and the program jumps to the next atom in the array. If the energy of the atom falls below the value of E_{therm} (determined by the user as an input parameter), the program then ignores the subsequent trajectory of this slow atom and jumps to the next atom in the array.

All atom trajectories are calculated until the atom array is empty before the program moves

on to start the next new ion trajectory. Most cascades calculated using typical plasma conditions require a maximum of about 30 atom details to be stored at any one time in the array. Therefore, the size of this array is restricted to 100 elements deep (to allow some flexibility) by 4 wide. The program that performs these routines is called NED FORTRAN and is listed in full in Appendix VII.

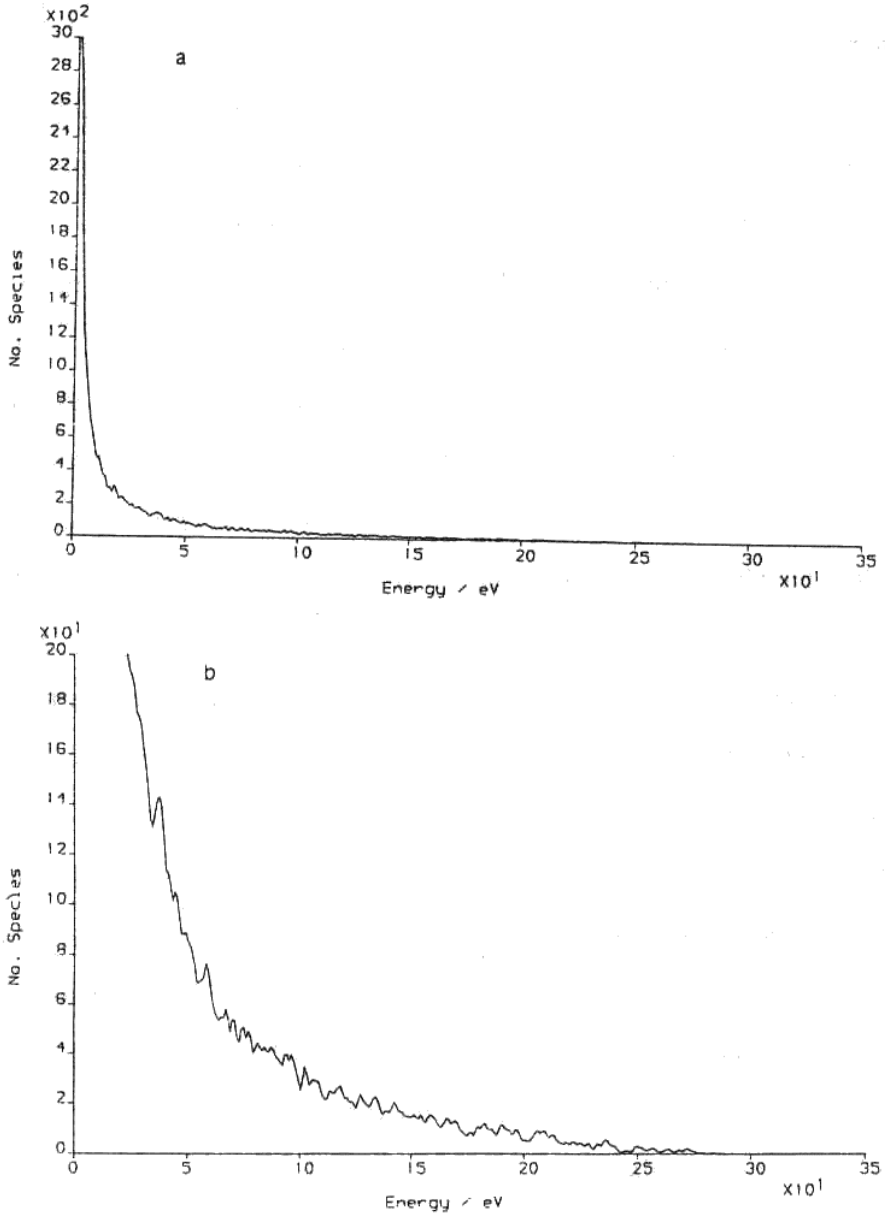

Fig.6.24. The NED corresponding to the standard high pressure plasma conditions, with E_{therm} = 0.1 eV. (a) the full NED, (b) an expanded scale. Note that 'No. Species' now means 'No. atoms', not ions.

6.12 Calculated NEDs and NADs

The NED and NAD obtained using the standard high pressure plasma conditions (table 6.1) have been calculated. For 10000 ions passing through the plane of origin, 44000 fast atoms struck the electrode. The NED is shown in fig.6.24a and also on an expanded scale in 6.24b. The curve resembles an exponential-type decay, with a sharp decrease in the number of atoms striking the electrode as the impact energy increases. The expanded plot shows that some atoms can strike the electrode with energies up to the maximum ion energy, E_2 (calculated from Equation (5.33)). These are atoms that had a collision very close to the electrode surface with an ion that had obtained nearly the maximum possible energy. The main point to note from this NED is that although most atoms strike the electrode with energies below 50 eV, a significant fraction impact with higher energies of several hundred eV. These fast atoms may play a very important role in etch mechanism, since they possess enough energy to cause sputtering with high efficiency. Even the lower energy atoms will have enough energy to cause bond-breaking reactions at the substrate surface, possibly leading to Dissociative desorption of reactive species, and hence etching. It is also likely that a significant cause of surface damage and substrate heating could be due to the impact of these fast neutrals rather than ions.

It is possible to combine the effects of IEDs and NEDs by recording the total number of particles striking the electrode, irrespective of whether the particle is an ion or an atom. These combined ion and neutral energy distributions will be termed INEDs, and the corresponding angular distributions INADs. The INED for the standard plasma conditions is shown in fig.6.25a and b. The structure between 220 and 280 eV is the IED corresponding to fig.6.15b. These diagrams make it very clear that the IED contains only a small fraction of the total number of energetic particles striking the electrode. Indeed, in fig.6.25a the contribution of ions to the INED is barely distinguishable from the large background NED. It seems that fast neutrals form the overwhelmingly major part of the total energetic particle distribution. For these plasma conditions, four times as many fast neutrals strike the cathode as ions, although in general the ions strike with higher energies.

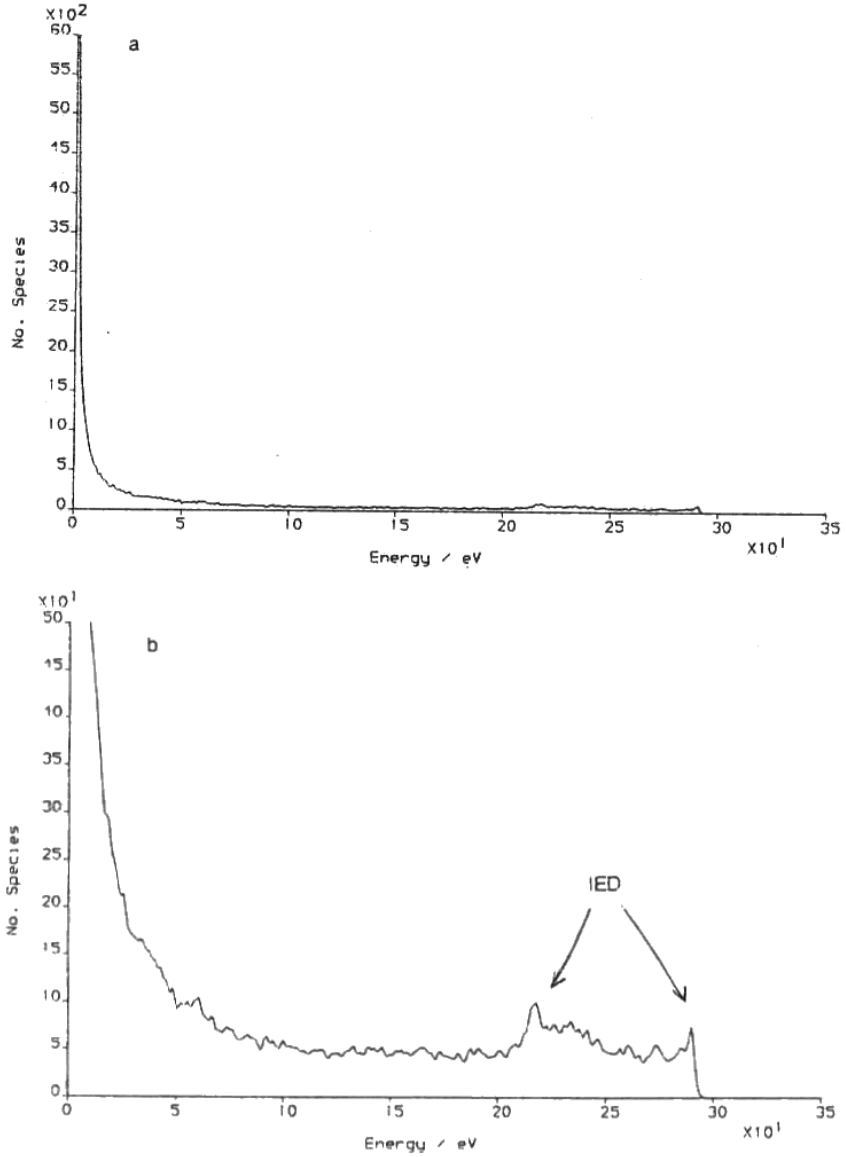

Fig.6.25. The INED corresponding to the standard high pressure plasma conditions, with E_{therm} = 0.1 eV. (a) the total INED, (b) on an expanded scale showing the contribution of the IED.

The NAD and INAD corresponding to the standard high pressure plasma conditions are shown in fig.6.26a and b. The NAD is composed of two sections; a peak at near normal incidence and a broad almost horizontal tail. The tail is indicative of an almost isotropic flux of particles to the surface (*i.e.* all impact angles have equal probability), and is due to atoms that have received their kinetic energy in scattering collisions with either ions or other fast atoms.

The peak at near normal incidence is caused by fast atoms that are created by charge exchange and then do not experience any further collisions before striking the electrode. This hypothesis was proven by repeating the NED simulation with no charge exchange interaction included in the model. In this case the normal incidence peak did not appear.

For the INAD, the contribution of the predominantly normal incidence ions increases the ratio of the height of the 90° peak to that of the broad distribution.

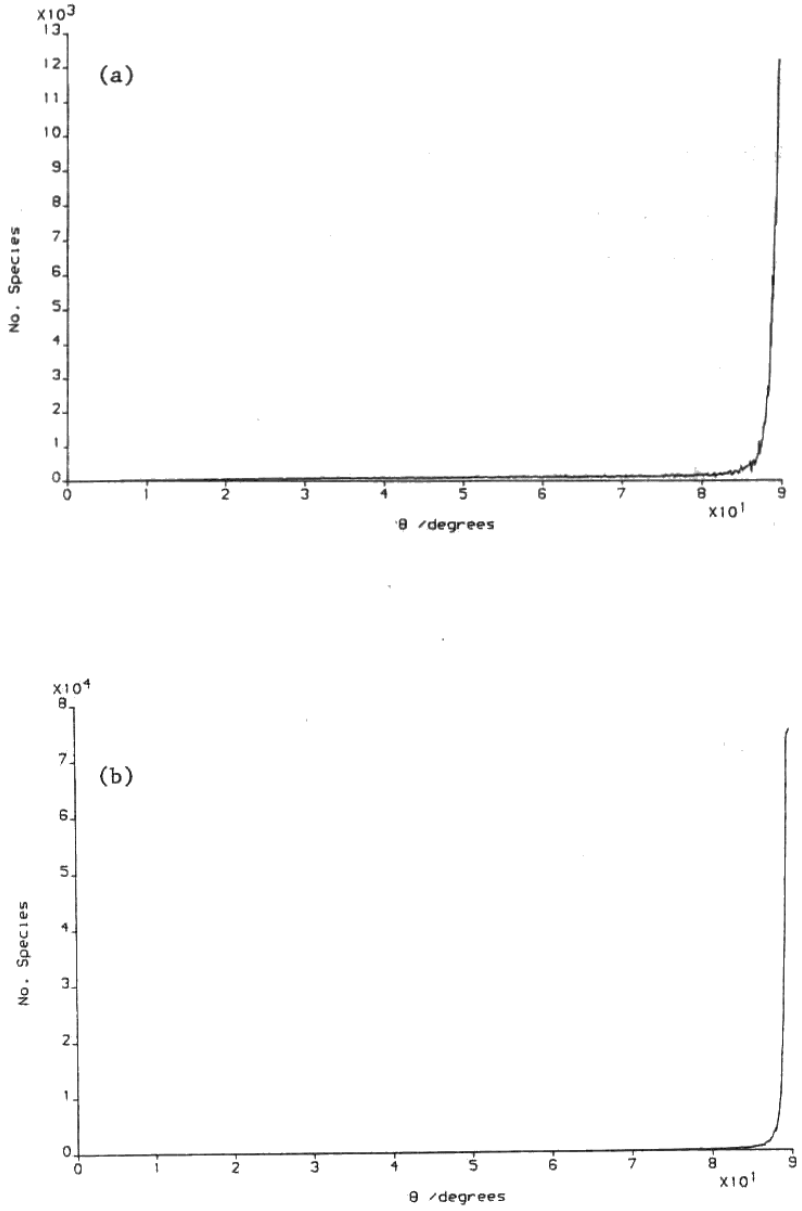

Fig.6.26. (a) NAD corresponding to fig.6.24.
(b) INAD corresponding to fig.6.25.

6.13 The Effect of Plasma Parameters Upon NEDs

In order to determine the sensitivity of the neutral particle distributions to plasma parameters, NEDs and NADs were calculated for varying conditions. Only the most important parameters have been studied.

6.13.1 E_{therm}

The value of E_{therm} is chosen by the program user. It determines the threshold energy below which the atom is considered to have reached thermal equilibrium with the bulk gas. The average thermal energy is about 0.04 eV (300 K), but E_{therm} can take any value around this average Boltzmann figure.

The value of E_{therm} was raised from 0.04 eV to 5 eV and the effects upon the calculated NEDs observed. A summary of the results is given in table 6.4. In effect, as E_{therm} is increased we exclude all the low energy atoms from the distribution. This has no effect upon the high energy part of the NED and the shape of the curve remains unchanged. However, increasing E_{therm} has a dramatic impact upon the required calculation time, since less atoms need to be calculated. If too large a value of E_{therm} (*e.g.* 5 eV) is chosen, however, the NED becomes less accurate and too much low energy atom data is lost. It is for this reason that 0.1 eV was chosen as the standard value for all NED calculations rather than 0.04 eV. Little data was lost by doing this, and computation time was greatly decreased.

E_{therm} /eV	Number of atoms	E_2 / eV
0.04	54667	280
0.1	44314	280
0.5	29625	280
1.0	25416	280
5.0	16858	280

Table 6.4. Variation of the number of atoms striking the electrode with varying values of E_{therm} all other conditions being standard (table 6.1). There were initially 10000 ions entering the sheath. E_2 is the maximum atom energy observed in the NED.

6.13.2 RF Voltage

The value of V_0 was varied from 100 to 500 V with all other plasma conditions being kept constant. The main results are given in table 6.5. As expected the maximum atom energy, E_2, seen in the NED was proportional to the RF voltage, since this energy is determined by the maximum ion energy observed in high frequency plasmas, and is given by Equation (5.33). Since for lower values of V_0, particles have in general less energy, the number of fast atoms will also be smaller than for larger values of V_0. The NAD did not change significantly with varying V_0.

V_0 / V	Number of atoms	E_2 / eV
100	38273	78
200	41634	160
300	43035	240
356	44314	280
400	44965	325
500	45809	410

Table 6.5. Variation in the number of atoms striking the electrode and maximum energy E_2 seen in the NED with varying V_0. 10000 ions originally entered the sheath.

6.13.3 Frequency

The NEDs and NADs were calculated for a variation in RF frequency from 100 kHz to 50 MHz. The observed NEDs did not change in form over this frequency range, remaining smooth decreasing curves with no discernible structure. For lower frequencies, ions in general have higher energies than at higher frequencies (see section 5.3.6). Therefore, fast atoms caused by collisions with these ions can exhibit energies up to the maximum value for low frequency plasmas of E_{max} given by Equation (5.13). The results of the NED calculations are given in table 6.6. The NADs showed no discernible change with varying frequency.

Frequency / MHz	Number of atoms	E_2 / eV
0.1	36065	580
1.0	49744	545
13.56	44314	280
50	44022	255

Table 6.6. Variation of the number of atoms striking the electrode and maximum energy E_2 seen in the NED with varying frequency. 10000 ions originally entered the sheath.

6.13.4 Pressure

As the pressure increases, the mean free path for both ions and atoms decreases. Consequently, there will be more collisions in the sheath. This will increase the number of fast atoms, but decrease the average energy per atom. The pressure was varied from 1 mTorr to 30 mTorr and the results of the NED calculations are given in table 6.7. Above 30 mTorr the number of fast atoms created by 10000 input ions exceeded the memory size of the computer array (100000).

Pressure / mTorr	Number of atoms	E_2 / eV
1	952	280
5	5411	280
10	13840	280
20	44314	280
30	93316	280

Table 6.7. Variation of the number of atoms striking the electrode and maximum energy E_2 seen in the NED with varying pressure. 10000 ions originally entered the sheath.

The main effect of pressure was noticed in the NADs rather than the NEDs, since E_2 remains constant as the pressure is increased. At low pressures, the NAD is dominated by a large near normal incidence peak due to atoms created in charge exchange processes. As the pressure increases these atoms begin to undergo scattering collisions with other gas atoms, so altering their trajectories away from the normal. Hence, as the pressure increases, the peak at near normal incidence decreases in proportion to the large scattered atom background. This is illustrated in fig.6.27a and b.

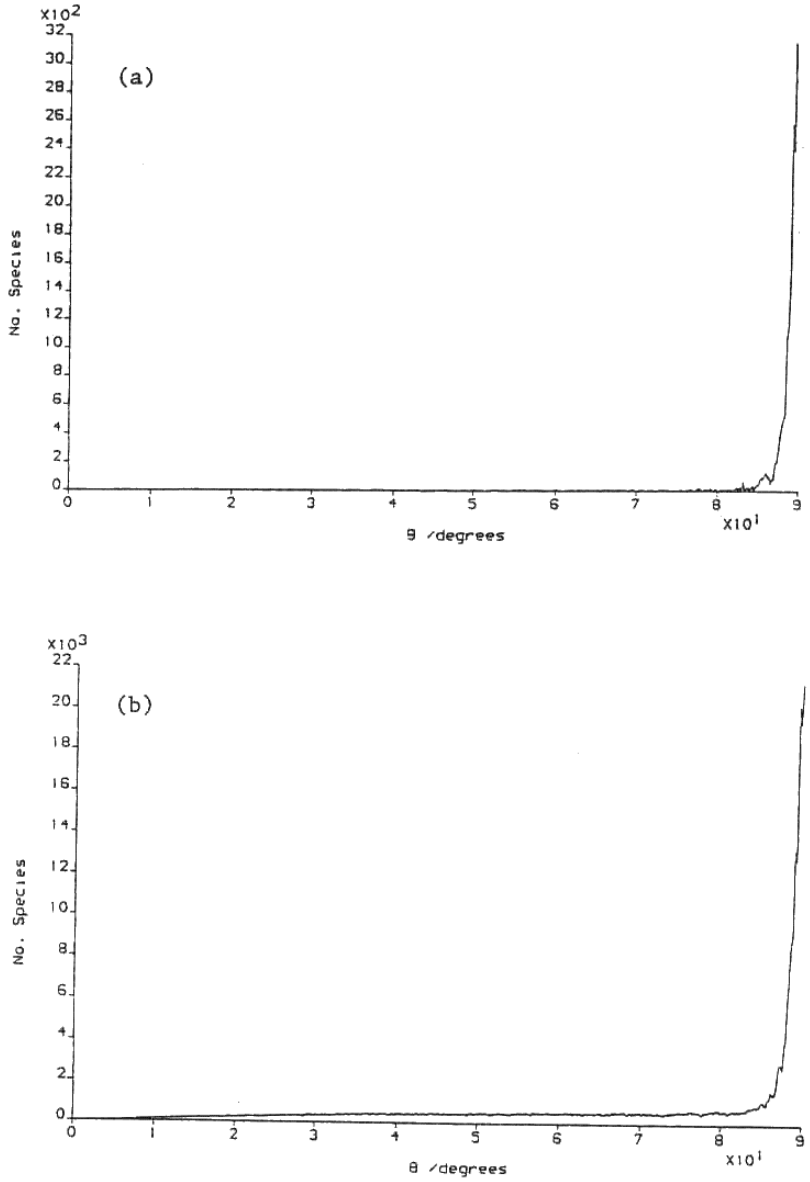

Fig.6.27. NAD for the standard high pressure plasma conditions at pressures of (a) 1 and (b) 30 mTorr.

6.14 Inelastic Collision Processes

Until now we have been treating Ar ions and atoms as isotropic hard-spheres undergoing elastic collisions. In other words, none of the kinetic energy of the fast species was converted into internal energy of either of the colliding species. If inelastic collisions are to be included in the model, there are two main processes that have to be considered; ionisation and excitation. These processes will now be dealt with in turn.

6.14.1 Collisional Ionisation

The two main processes we shall discuss are ionisation by ion and atom impact upon Ar atoms:

$$Ar^+(\text{very fast}) + Ar(\text{slow}) \rightarrow Ar^+(\text{fast}) + Ar^+(\text{fast}) + e$$

$$Ar(\text{very fast}) + Ar(\text{slow}) \rightarrow Ar^+(\text{fast}) + Ar(\text{fast}) + e$$

We need to examine whether these processes will be significant in the sheath. McDaniel [189] states that for heavy particle collisions (*e.g.* Ar), the threshold energy for ionisation is about two times higher than the ionisation energy of the particle which loses the electron. For Ar, the ionisation potential is 15.759 eV, which means that a collision energy of at least 30 eV is required to produce ionisation. This immediately shows that collisional excitation will not occur in anode sheaths which rarely produce ion energies of greater than 30 eV. Therefore, we need only consider cathode sheaths.

Energy / eV	***P*(atom-atom)**	***P*(ion-atom)**
0	0	0
10	0	0
50	0	0
100	0.007	0.0014
200	0.0173	0.0075
300	0.0276	0.020
400	0.0350	0.0256

Table 6.8. The probability of ionisation, *P*, in atom-atom and ion-atom collisions as a function of collision energy for Ar plasmas.

The cross-section for this type of ionising collision increases with collision energy and peaks in the tens of keV region. Below this peak, in the energy range appropriate to RIE (*i.e.* 0 to 500 eV), the relative velocity of the colliding particles is small compared to the velocity of the orbiting electrons. Therefore the cross-section is small, since the electrons have sufficient time to adjust adiabatically to the slowly-changing perturbation. The curves of cross-section for ionisation versus energy for Ar^+-Ar and Ar-Ar collisions are given in fig.6.28a and b. It can be seen from these diagrams that the ionisation cross-sections for the typical energies of particles in RIE reactors is about 1 $Å^2$, which is about 1% of those for scattering or charge exchange. By comparison of the magnitudes of the cross-sections for ionisation, scattering and charge exchange at different energies, the probability that a collision of a certain energy will result in ionisation (rather than either of the other processes) has been calculated, and is presented in table 6.8.

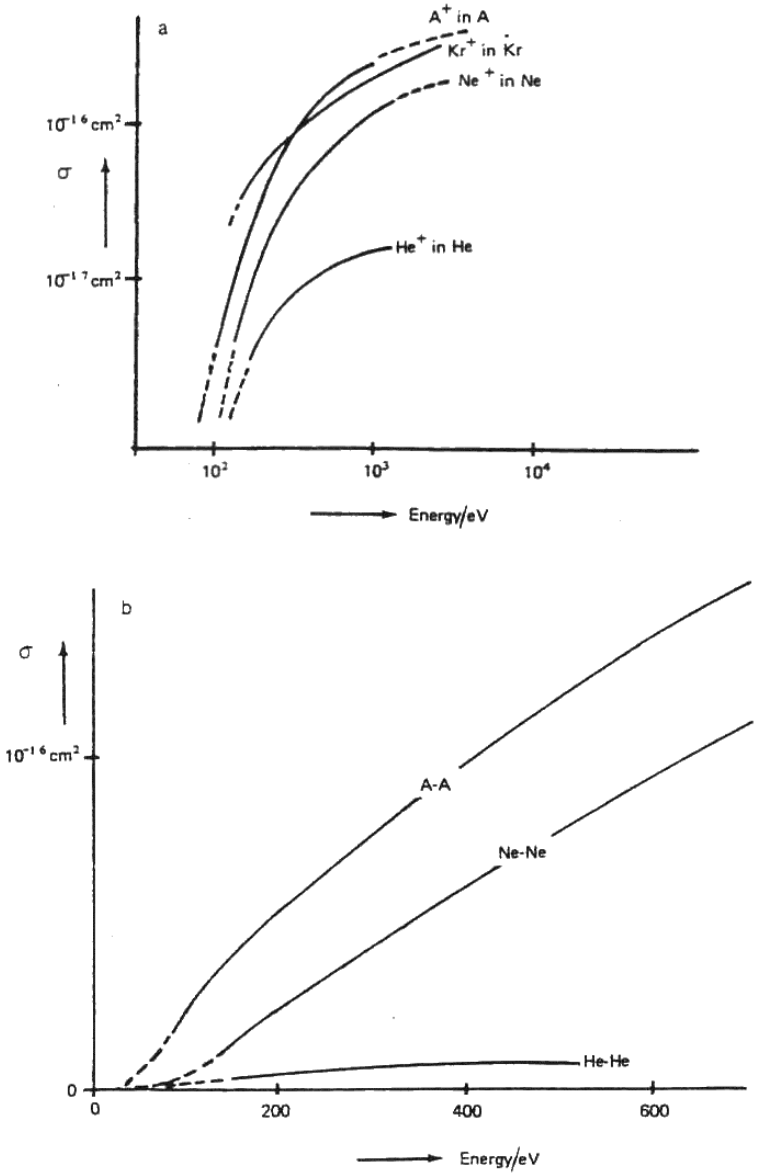

Fig.6.28. Cross-section for ionisation by (a) ion impact and (b) atom impact for noble gases as a function of impact energy (after ref.[47]).

Using the Monte Carlo program, it has been calculated that for the standard high pressure plasma conditions, 90% of atom-atom collisions occur with a collision energy < 50 eV. Let us assume ~ 50 eV is the threshold impact energy for ionisation. Then for 10000 fast atom collisions in the sheath, the expected number of new ions created by atom impact will be approximately given by

No. new ions = (No. collisions) × (fraction with $E > 50$ eV) × (probability of ionisation)

= $10000 \times 0.1 \times 0.01\text{-}0.02$ = 10-20 new ions.

Again, using the Monte Carlo program we calculate that about 50% of ion-atom collisions occur with $E < 50$ eV. Accordingly, the corresponding number of new ions created by ion impact will be

= $10000 \times \sim 0.5 \times 0.01\text{-}0.02$

= 50-100 ions

Thus, estimates show that it is a valid first order approximation to say that ionisation by fast atom-atom or ion-atom collisions is not an important process in the sheath. However, it would be a relatively straight forward process to include these ionisation phenomena in the Monte Carlo program to check whether this approximation is justified. This has not yet been done, and may form the basis for future work.

6.14.2 Collisional Excitation

McDaniel [189] states that when a heavy particle passes through matter a substantial fraction of its energy is dissipated in the excitation of atomic and molecular states of target particles and sometimes of the incident particle itself. Unfortunately, very little information is available about the excitation cross-sections for typical process gases, including Ar. Most data is available only for gases such as He, H_2 and N_2 (see ref.[210-212] and others in McDaniel [891]). Various workers have measured the cross-section for excitation of Ar into specific excited states by Ar^+ impact and obtained values of σ of about 10^{-3} Å^2 for collision energies of a few eV [213-217]. Furthermore, von Engel [118] states that charge exchange processes are likely to be accompanied by excitation.

For the purposes of calculating excitation phenomena in the Monte Carlo program, we require the probability that a collision of a certain energy will be inelastic rather than elastic. In other words we require the *total excitation cross section* and the probability of producing any given excited state for any collision energy. These data are not available, and are also not readily calculated, and so we must try another approach. If we wish to ascertain whether excitation significantly affects IEDs or NEDs, it is worth considering the two extreme cases. We have already dealt with one of these, namely the 100% elastic collision scenario, where the probability of excitation is zero. The other extreme is to say that *every* ion-atom or atom-atom collision above a threshold energy is inelastic, so that the probability of excitation is then 1. Using this assumption we can obtain IEDs and NEDs with which to compare previous distributions.

However, we still need a method to determine how much of the collision energy is converted into internal excitation energy of one of the species. We shall assume for simplicity that only the initially slow moving target atom is excited by the impact of a fast moving ion or atom. A grossly simplified diagram of the energy levels of Ar is shown in fig.6.29. The ground state is at 0 eV and there is an 11.55 eV gap before the first excited state appears. There are then numerous

other excited states increasing in energy until the ionisation limit is reached at 15.759 eV.

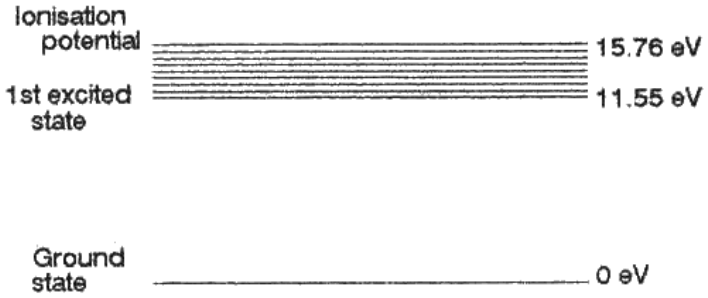

Fig.6.29. Simplified diagram of the energy levels of Ar.

From the Uncertainty Principle, if a collision takes a time, τ, to occur, the energy levels will be 'blurred out' to a certain extent given by

$$\Delta E = h/(2\pi\tau) \tag{6.43}$$

If we approximate the collision time by

$$\tau = a / v \tag{6.44}$$

where a is the radius of a typical atom (say ~ 2 Å) and v is the collision velocity, we obtain that for collision energies of 0.1, 15 and 500 eV every energy level of Ar will be blurred by 0.002, 0.03 and 0.16 eV, respectively. Therefore, it is reasonable to say that for higher energy collisions we can represent the Ar atom energy levels as a diffuse 'energy band' between 11.55 and 15.76 eV.

The collision can then be envisaged as a three stage process.

(i) As the fast ion (or atom) approaches the target atom the electron clouds of the two species begin to interact with each other and the pair form a pseudo-dimeric transition state.

(ii) The kinetic energy of the ion (or fast atom) is then redistributed into the transition state, resulting in an electron being promoted to an excited state.

(iii) The transition state then dissociates with the two Ar species flying apart, each with a proportion of the dimer's remaining energy.

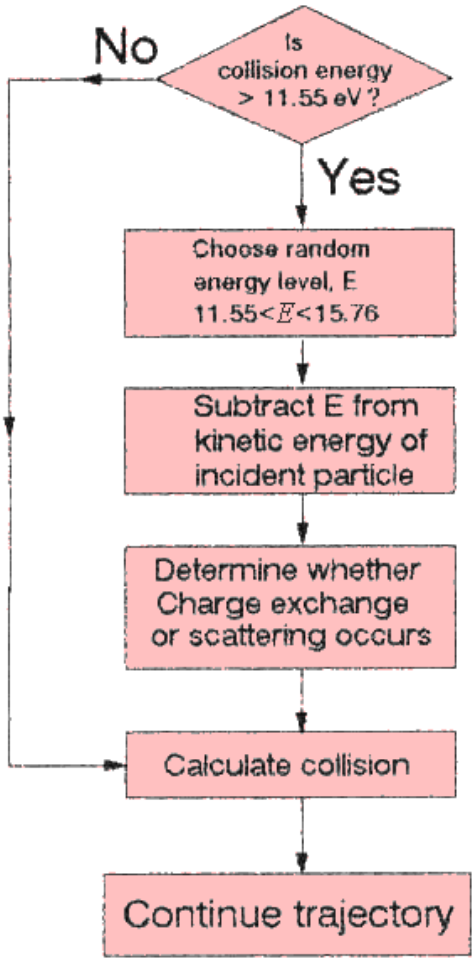

Fig.6.30. Flow chart for inelastic collisions.

This process has been modelled in the following way (see fig.6.30). First, the collision energy is examined to determine whether excitation is energetically possible.

If the collision energy < 11.55 eV, no excitation can occur, so the collision is treated as elastic using the procedures outlined in sections 6.2-6.2.5.

All collisions with energy > 11.55 eV are now said to cause excitation. A random excitation energy is now chosen from a linear probability distribution between the first excited state and the ionisation energy. This excitation energy is then immediately subtracted from the collision energy of the incoming particle before the post-collision dynamics are calculated.

The type of collision is then determined. For ion-atom collisions both charge exchange and scattering can occur, with probabilities given by the ratio of the cross-sections for each of these 2 processes at the collision energy (see section 6.2.4). For atom-atom collisions, only scattering can occur.

If scattering is deemed to occur, the new scattering angles and post-collision trajectories of both the collision partners are calculated using the procedures outlined in sections 6.2-6.2.5, but with the reduced collision energy.

For charge exchange a similar procedure is followed, so that the incoming ion is not only

neutralised but also excited as the electron transfers directly into an excited state. This process creates an effectively stationary ion and a fast moving excited atom. Since some of the kinetic energy of the ion has been converted to excitation of the atom, after the charge transfer is complete the fast atom continues along the same trajectory as the ion would have followed, except with a smaller velocity.

As long as the excited atom is not metastable (see section 6.14.3d), the atom will radiate back to the ground state very quickly. Radiation will occur long before any further collisions can take place (see section 4.7.1).

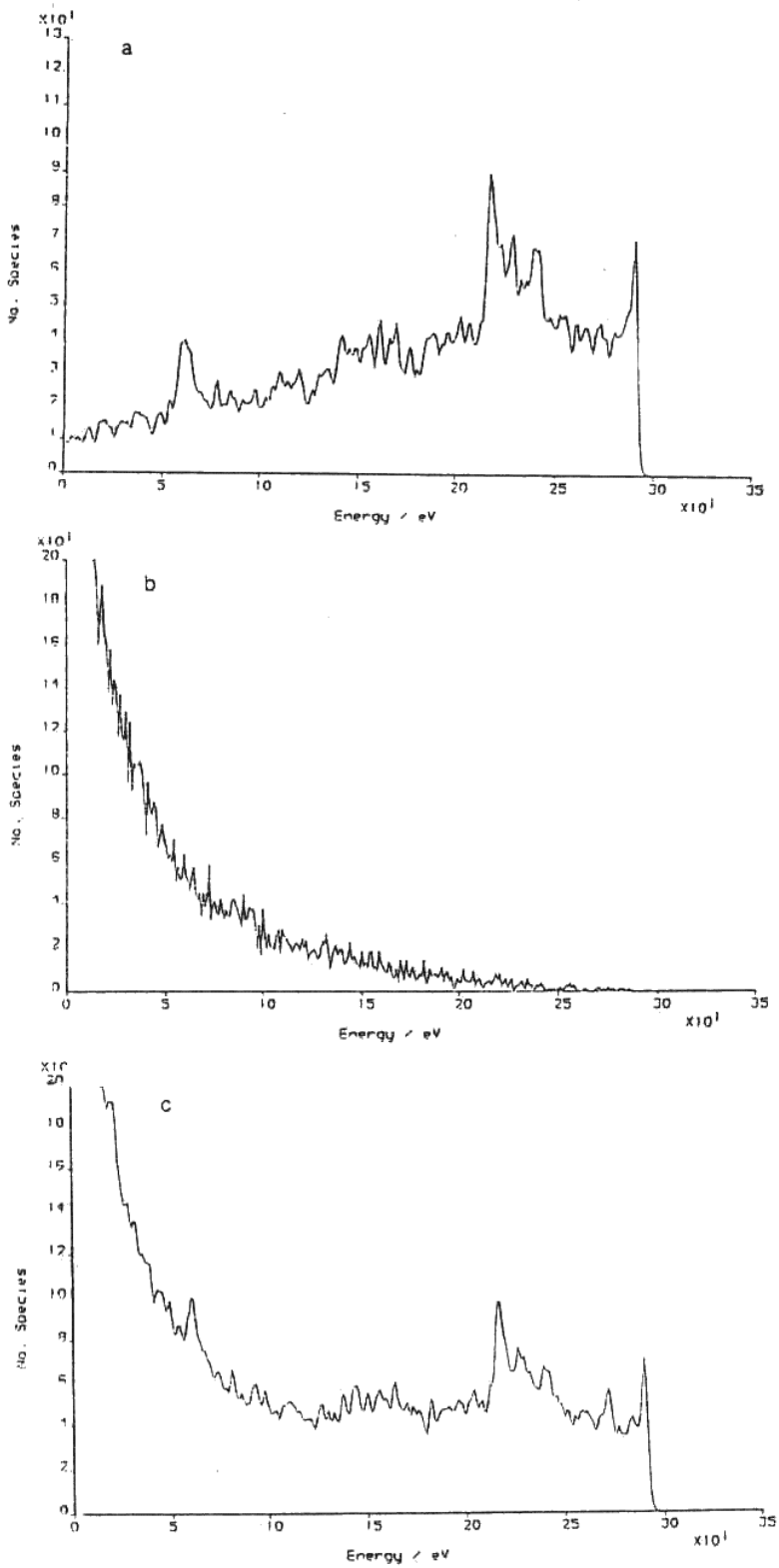

Fig.6.31. Energy distributions using the standard high pressure plasma conditions incorporating the inelastic collision model, (a) IED, (b) NED, and (c) INED.

Using the model described above, the IED, NED and INED including inelastic collisions have been calculated and are shown in fig.6.3 l(a-c). The main point to note is that the inclusion of inelastic collisions has not significantly changed any of these distributions. The angular distributions (IAD, NAD and INAD, not shown) are also virtually identical to those calculated using only the elastic collision model. What little effect there is has been mainly to reduce the number of fast atoms striking the electrode by about 20%, and to reduce the proportion of atoms having high energy.

Since the distributions calculated using the inelastic and elastic collision models are very similar, it can be stated that inelastic collisions make very little difference to high pressure particle distributions. Moreover, the real probability of inelastic collisions will be much less than 1, so that in reality inelastic collisions will have even less effect than seen here.

6.14.3 Other Inelastic Processes

There are many other inelastic collision processes that have not been included in the model for ion and neutral trajectories within the sheath. Most of these are minority processes which will not significantly affect calculated IEDs and NEDs, but they are still worth mentioning.

(a) **Vibrational/Rotational Excitation**: these will not apply to a monatomic Ar plasma, but will become a very important energy loss mechanism for more complex gas plasmas.

(b) **Double ionisation**: this is a process such as

$$Ar^+ + Ar \rightarrow Ar^{2+} + Ar + e$$

These reactions are much rarer than single ionisations [118] due to the large second ionisation potential of Ar (27.63 eV [163]).

(c) **Dimerisation**: Ar can temporarily dimerise in a process such as

$$Ar^+ + Ar\ (+M) \rightarrow Ar_2^+$$

where M is a third body or surface. This occurs to an insignificant extent in Ar plasmas [189].

(d) **Metastable species**: these are excited atoms (or ions) that have a very long lifetime to fluorescence. Consequently, they may undergo collisions *before* they radiate. Since the amount of energy needed to ionise an already-excited atom is relatively small, metastable species might provide a ready method to produce ions in the sheath. Metastable energy levels of Ar are well known (see section 7.3.1.2), but their concentration is small compared to that of the ground state Ar atoms. Hence, fast ions or atoms will collide with ground state atoms much more frequently than metastables, and so we can safely ignore such interactions.

(e) **Two Species Excitation**: such as

$$Ar^{+} + Ar \rightarrow\!\!\!\!- \; Ar^{+*} + Ar^{*}$$

$$Ar + Ar \rightarrow Ar^{*} + Ar^{*}$$

These processes are much rarer than single excitation [118]. Also, it would be extremely difficult to model such processes since the relevant data are not known.

(f) **Other Ionisation Processes in the Sheath**: these processes are not well understood and require more study. They include

(i) Ionisation of Ar atoms by the electrons in the high energy tail of the Maxwell-Boltzmann distribution during the parts of the RF cycle where the sheath is at a minimum thickness. This process could produce new ions at any point in the sheath between the minimum and maximum sheath thicknesses.

(ii) Ionisation by fast secondary electrons these electrons are caused by ion, electron or metastable species impacting upon the electrode. The emitted electrons are then accelerated through the sheath into the plasma region (see section 7.3). These fast electrons can collide with neutral Ar atoms in the sheath region and cause ionisation. However since the number of secondary electrons is expected to be small [47], this process should not be a significant source of Ar^{+} production.

(iii) Photoionisation: High energy (UV) photons may also cause ionisation in the sheath region (see section 7.3.1.4). These processes are still not well understood in RF reactors. Some workers have found that photoelectric yields can be as high as yields from ion impact under certain conditions [218]. However, in order to simulate photoionisation we would need the photon fluxes and frequency distribution throughout the sheath region, data which are not readily obtainable. Therefore, this process has not been included in any modelling to date, although it may be included in future work.

6.15 Backscattered Atoms

Some fast atoms created by collisions in the sheath region may be travelling away from the electrode. If these atoms pass through the plane of origin they will leave the sheath and enter the bulk of the plasma region. Since it is impracticable to model the entire plasma region, any particles leaving the sheath are normally ignored by the computer program. This process is termed *backscattering* and is analogous to a sputtering mechanism, where the 'target' is the sheath region and the surface is the plane of origin. As we have mentioned in section 6.2.4, positive ions can also be backscattered from the sheath, although this process is much more unlikely than for atoms since the electric field pulls ions towards the electrode.

It is worthwhile looking briefly at the energies of atoms that are backscattered from the sheath. The main motivation for this study was to ascertain whether this could be a possible mechanism for fast excited atom production, and hence produce an explanation for the Fabry Perot Interferometry (FPI) results given in Chapter 4. Backscattered Ar atom energies were first calculated using the standard elastic collision model and then the purely inelastic model of

section 6.14.2. This required a slight modification to the program so that the energy and angles of atoms passing through the plane of origin were stored, rather than the data for those that struck the electrode.

6.15.1 Elastic Collision Model

Using elastic collisions only, the backscattered atom energy distribution (BAED) and angular distribution (BAAD) for the standard high pressure plasma conditions are shown in fig.6.32a and b. For 25000 input ions, 138374 atoms struck the electrode, but 70659 atoms were backscattered into the plasma region. Most of these backscattered atoms had very low energy, the average energy being ~ 0.49 eV. This value for average energy is very similar to that observed for fast Cl^* atoms in Chapter 4. We shall return to this point in the next section. The BAED is a smooth decay curve between 0 and about 3.5 eV.

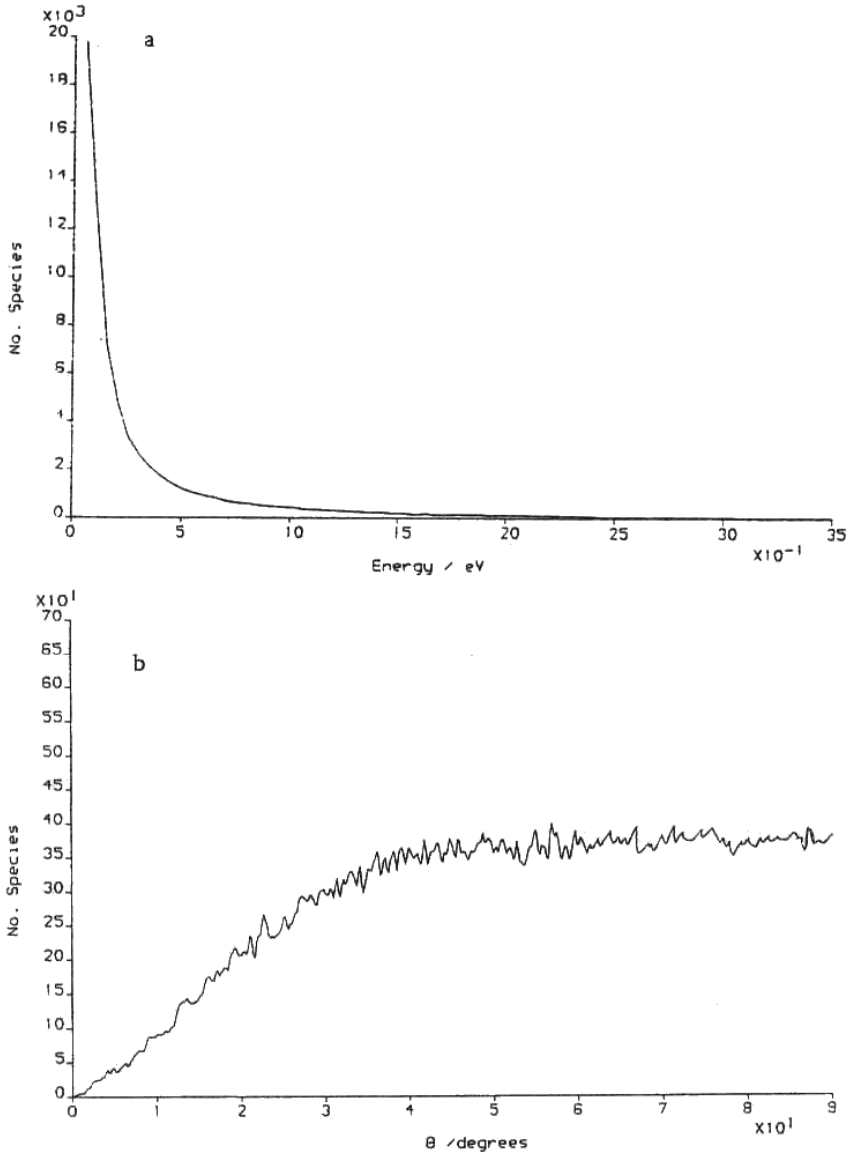

Fig.6.32. (a) BAED and (b) BAAD for the standard high pressure plasma conditions.

The BAAD shows that these atoms leave the sheath with an almost isotropic distribution. For angles above 40°, the BAAD shows a horizontal distribution indicative of an isotropic flux, but this curve tails off to zero by 0° indicating that the distribution is not completely isotropic. The reason that the distribution is not completely isotropic is that the atoms have not yet reached thermal equilibrium (as evidenced by their higher than normal energies). At higher pressures it is expected that the distribution should be completely isotropic.

Another reason for the drop off in the distribution at low angles is due to collisional effects. Fast atoms produced at a certain point in the sheath that are travelling at near normal angles of incidence pass through the plane of origin unimpeded, but atoms which are produced at the same point in the sheath, but which are travelling at shallower angles have to travel much further

before encountering the plane of origin. Therefore, atoms with shallow trajectories stand a larger probability of undergoing another scattering collision before passing back through the plane of origin. A scattering collision will deflect the trajectory of the atom, so that on average the angle of incidence will be increased away from the previous glancing angle. Therefore, shallower angles are discriminated against and the BAAD curve tends to zero at very glancing angles. This effect is a function of the velocity of the ion normal to the plane of origin, *i.e*. it is proportional to sin θ. If this sin θ term is divided out of the curve, we obtain a near horizontal line down to 0°.

The conclusions are that the sheath produces an almost isotropic flux of atoms entering the plasma region with energies of a few tenths of an eV. This could be a way of distributing energy from the sheath region into the plasma bulk.

6.15.2 Inelastic Collision Model

The backscattered atom data were recalculated using the model for inelastic collisions described in section 6.14. Both the BAED and BAAD were virtually identical to those seen for the elastic collision model. However, as expected, the average energy of backscattered atoms was reduced to ~ 0.28 eV, a value even more similar to those seen in Chapter 4. Also, the total number of backscattered atoms dropped by 39% to 43293 (for 25000 input ions). So the inelastic model predicts less atoms backscattered, with, in general, less energy.

The value for the average kinetic energy predicted by this model is very similar to that seen for excited Cl^* atoms using FPI. This forms the basis of a hypothesis that maybe the fast atoms seen in Chapter 4 were atoms backscattered from the sheath that had subsequently been excited by electron impact. To test this theory, the computer program was used to predict the average energies of backscattered atoms as some of the plasma parameters were varied. This will not be a very accurate prediction, since we are assuming Ar will behave similarly to Cl, but the trends should be qualitatively similar.

The first parameter varied was RF voltage, which is directly related to the RF power. The results are given in table 6.9 for 25000 input ions. These results show that so long as V_0 is above a threshold value, the average energy is independent of V_0. This is in direct contrast to the Fabry Perot observations, which showed a linear dependence of energy upon RF power for all species monitored. The computer predictions also show that the number of backscattered atoms increases with V_0, and thus that the intensity of any emission line should increase with V_0, which agrees with experimental observations.

V_0 / V	Average Energy / eV	No. atoms
100	0.24	3352
200	0.28	12920
300	0.28	43293
400	0.28	88969

Table 6.9. Number and average energy of backscattered atoms with increasing V_0 for the standard high pressure plasma conditions.

Another parameter varied in Chapter 4 was the frequency. Therefore, the computer simulation was used to calculate the average energy of backscattered atoms at different

frequencies, with the results being given in table 6.10. It can be seen that at very low frequencies the average atom energy decreases as the frequency increases, but above about 10 MHz the average energy remains constant. Also, the number of backscattered atoms is approximately independent of frequency. Both these predictions agree with the FPI observations. Since only a small range of frequencies was used in those experiments, neither the observed energy nor intensity were affected by frequency.

Frequency / MHz	Average Energy / eV	No. atoms
0.1	0.44	44819
1	0.32	44971
5	0.30	45572
10	0.28	43486
13.56	0.28	43293
50	0.28	42104

Table 6.10. Average energy and number of backscattered atoms calculated for varying frequency using the standard high pressure plasma conditions.

In the FPI work, one of the most puzzling results was the increase in average energy of Cl^* atoms with increasing pressure. To see if the backscattered atom hypothesis predicts this observation the computer simulation program was run for different pressures and the results are given in table 6.11. The simulation predicts the opposite to what is seen experimentally, *i.e*. that the average energy of backscattered atoms *decreases* with increasing pressure. Therefore, we can say that the hypothesis that backscattered atoms are the cause of the hot excited Cl^* atoms observed in Chapter 4 is incorrect.

Pressure / mTorr	Average Energy / eV	No. atoms
1	0.63	21
5	0.53	574
10	0.44	3063
20	0.28	17086
30	0.22	42272
50	0.16	99819

Table 6.11. Number and average energy of backscattered atoms with increasing pressure using the standard high pressure plasma conditions.